The Journal of Chemical Physics ARTICLE scitation.org/journal/jcp

Multilayered allosteric modulation of coupled folding and binding by phosphorylation, peptidyl-prolyl *cis/trans* isomerization, and diversity of interaction partners

Cite as: J. Chem. Phys. 157, 235102 (2022); doi: 10.1063/5.0128273
Submitted: 27 September 2022 • Accepted: 28 November 2022 •
Published Online: 21 December 2022

Karin J. Buholzer,[1] Jordan McIvor,[2] Franziska Zosel,[1,a)] Christian Teppich,[1] Daniel Nettels,[1] Davide Mercadante,[1,2,b)] and Benjamin Schuler[1,3,b)]

AFFILIATIONS

[1] Department of Biochemistry, University of Zurich, Zurich, Switzerland
[2] School of Chemical Sciences, The University of Auckland, Auckland, New Zealand
[3] Department of Physics, University of Zurich, Zurich, Switzerland

Note: This paper is part of the JCP Special Topic on New Views of Allostery.
[a)] **Present address:** Department of Biophysics and Injectable Formulation 2, Novo Nordisk A/S, Måløv, Denmark.
[b)] **Authors to whom correspondence should be addressed:** davide.mercadante@auckland.ac.nz and schuler@bioc.uzh.ch

ABSTRACT

Intrinsically disordered proteins (IDPs) play key roles in cellular regulation, including signal transduction, transcription, and cell-cycle control. Accordingly, IDPs can commonly interact with numerous different target proteins, and their interaction networks are expected to be highly regulated. However, many of the underlying regulatory mechanisms have remained unclear. Here, we examine the representative case of the nuclear coactivator binding domain (NCBD) of the large multidomain protein CBP, a hub in transcriptional regulation, and the interaction with several of its binding partners. Single-molecule Förster resonance energy transfer measurements show that phosphorylation of NCBD reduces its binding affinity, with effects that vary depending on the binding partner and the site and number of modifications. The complexity of the interaction is further increased by the dependence of the affinities on peptidyl-prolyl *cis/trans* isomerization in NCBD. Overall, our results reveal the potential for allosteric regulation on at least three levels: the different affinities of NCBD for its different binding partners, the differential modulation of these affinities by phosphorylation, and the effect of peptidyl-prolyl *cis/trans* isomerization on binding.

INTRODUCTION

Intrinsically disordered proteins (IDPs) have important regulatory roles in signal transduction, transcription, and cell-cycle control.[1–4] Many advantages of structural disorder in cellular regulation have been proposed, among them structural flexibility, which allows IDPs to interact with many different binding partners and leads to higher accessibility for posttranslational modifications (PTMs).[5–8] The degree of disorder in unbound IDPs and even in their complexes varies greatly, from largely ordered to fully disordered.[4,9,10] Structural disorder enables or facilitates various types of allosteric regulation.[11] In general, folding-coupled binding processes, which have been observed for many IDPs,[12,13] fall into the class of allosteric changes if we consider allostery as a ligand-induced conformational change in a protein that modulates its biological function, including the thermodynamic coupling of binding and folding in multidomain IDPs.[14] Other allosteric processes common for IDPs are the competition between different interaction partners for overlapping binding sites[11,15] and the effects of PTMs on structure and affinity.[16,17] However, many of the allosteric mechanisms in IDPs and their interplay remain to be understood quantitatively.

IDPs are particularly prevalent among transcription factors.[18] A prominent example is the CREB-binding protein (CBP), an important hub in transcriptional regulation, with more than 400 known binding partners.[6] It consists of eight domains connected by long flexible linkers. In view of its modular architecture, CBP has been suggested to act as a signal integrator by combining the interactions and corresponding signals of the individual domains.[6] The C-terminally located nuclear coactivator binding domain (NCBD), a member of the large group of αα-hub domains,[19] has an interesting property: It contains three α-helices but lacks a stably folded core,[20–22] which enables the helices to be present in different arrangements within the conformational ensemble.[21,22] Many proteins have been reported to bind to the region of CBP encompassing NCBD,[23–25] and for eight well-characterized cases, the NCBD core region (CBP 2058–2116) is sufficient for the interaction.[20,22,26,27] Among them are five IDPs: the three homologous nuclear receptor coactivators (NCoAs) SRC1 (the steroid receptor coactivator 1), TIF2 (the transcriptional intermediary factor 2), and ACTR (the activator for thyroid hormone and retinoid receptor); the transactivation domain of the tumor suppressor p53, p53TAD; and the adenoviral early region 1A protein, E1A. The available structures reveal different arrangements of the three helices of NCBD when bound to different binding partners[20,26,28,29] [Fig. S1(a)], which illustrates the conformational plasticity of this IDP that enables its versatile interactions.

Among the interactions of NCBD, binding to ACTR has attracted special attention because it was the first reported example of two IDPs that bind and fold in a mutually synergistic manner.[20] Since then, many studies have investigated this binding mechanism and have revealed remarkable structural, energetic, and kinetic aspects of NCBD binding to several of its binding partners.[30–40] Here, we investigate the various levels of regulation that may be involved in these interactions: the different affinities of NCBD with its different binding partners; how they are differentially affected by peptidyl-prolyl *cis/trans* isomerization; and the role of NCBD phosphorylation, which is known to occur *in vivo*.[41–44] Specifically, we focus on the interaction of NCBD with three of its intrinsically disordered binding partners: the three NCoAs ACTR, SRC1, and TIF2. We find that the phosphorylation of Ser residues near Pro20 reduces the affinity of NCBD to all three NCoAs, but to different extents. We further identify peptidyl-prolyl *cis/trans* isomerization of Pro20 of NCBD to be an important kinetic modulator for the interaction with ACTR and TIF2, but less so for SRC1. These results point toward a complex interplay of these allosteric processes and their potential role for cellular regulation.

RESULTS

Affinity of NCBD to different binding partners

NCBD can bind both to intrinsically disordered and to folded proteins. Nuclear magnetic resonance (NMR) structures indicate that the arrangement of the three helices of NCBD bound to its disordered binding partners is similar but not identical; the detailed arrangement of the helices and the length of the third helix, e.g., differs between the bound structures[20,21,26,28,45] [Figs. 1(a) and S1(a)]. Different binding partners/effectors thus lead to different functional conformations, in line with the concept of allostery. The detailed

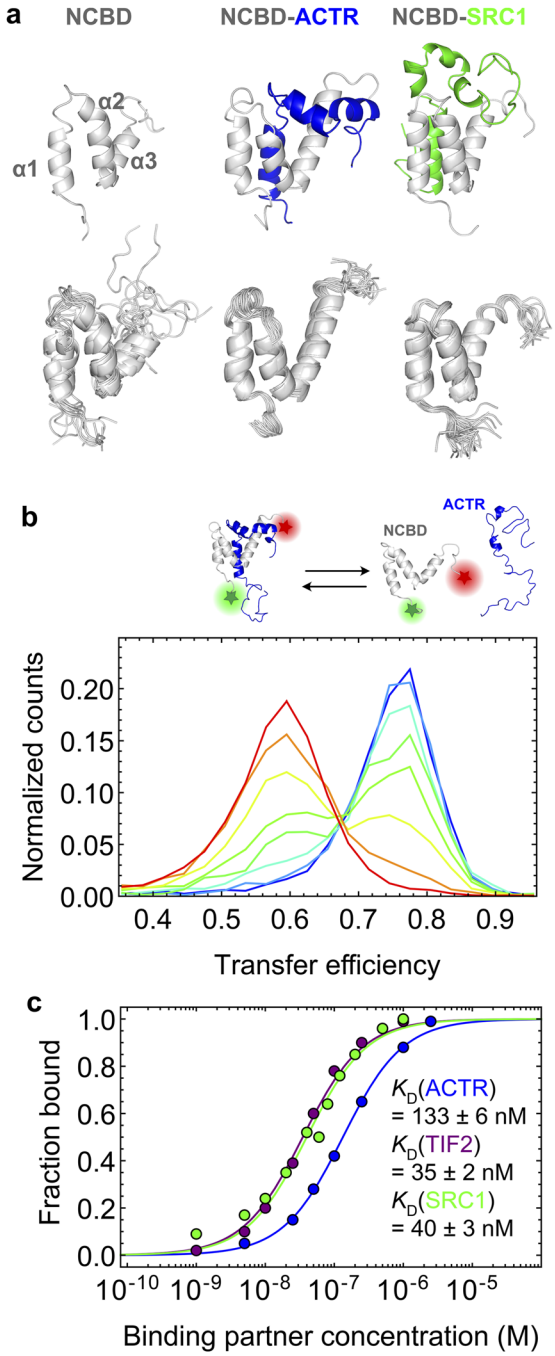

FIG. 1. Binding of NCBD to its disordered interaction partners. (a) NMR structures of free NCBD (gray, with helices α1-α3 indicated), NCBD bound to ACTR (blue) or SRC1 (green). To highlight the different degrees of disorder in the flexible tails of NCBD, NMR conformers of the respective structures of NCBD are overlaid below (PDB 2KKJ,[21] 1KBH,[20] 2C52[26]). (b) Normalized single-molecule FRET efficiency histograms from a titration of fluorescently labeled NCBD (Alexa Fluor 488 and CF660R, green and red stars) with unlabeled ACTR [increasing concentration from blue to red; see panel (c) for concentration range]. (c) Fractions of bound NCBD as a function of binding partner concentrations (see the legend), fitted with binding isotherms. Uncertainties represent standard errors of the fits.

structure of NCBD in complex with TIF2 is unknown, but in view of its high sequence identity with ACTR (75% in the interacting helical region of ACTR (1044–1077[20]) and the corresponding residues in TIF2, Table S1), it is likely to adopt a similar conformation. To study the interactions of NCBD binding to its disordered partners, we first conducted free-diffusion single-molecule Förster resonance energy transfer (FRET) experiments with NCBD labeled at its termini with Alexa Fluor 488 and Biotium CF660R. This dye pair is well suited for monitoring the relatively short distances between the termini because of its relatively small Förster radius of R_0 = 4.6 nm (see Methods).[38]

In the absence of a binding partner, we observe a single peak in the transfer efficiency histogram of NCBD [Fig. 1(b), blue curve]. Addition of unlabeled ACTR leads to the population of a second peak at lower transfer efficiency [Fig. 1(b)], indicating an increased end-to-end distance of NCBD in complex with ACTR, which is in line with the C-terminus of NCBD gaining structure and extending its third helix upon complex formation[20,22] [Fig. 1(a)]. We find similar shifts for the binding of NCBD to TIF2, and SRC1, albeit with slightly different transfer efficiencies (Fig. S2), consistent with the slightly different conformations of NCBD in its different complexes [Fig. 1(a)]. From the relative peak areas, we obtain the fraction of bound NCBD as a function of binding partner concentrations and quantify equilibrium dissociation constants, K_D [Fig. 1(c)]. All NCoA-NCBD complexes exhibit tight binding in the nanomolar range, with slightly lower affinity for ACTR than for SRC1 and TIF2, in agreement with previous results.[40] We also confirmed the lower, micromolar affinities previously reported for p53TAD and E1A[40,46] (Fig. S2) but did not investigate them further because of the high affinity required for dissecting the kinetics in detail with intermolecular FRET experiments. These differences in affinity provide an obvious first level of regulation: The effects of different binding partners will manifest at different concentrations, which can be tuned by changes in protein turnover.

NCBD phosphorylation reduces binding affinity

Another well-established mechanism of regulating protein interactions is by posttranslational modification. NCBD is known to be phosphorylated at several sites *in vivo*, including Ser residues near Pro20[41–44] [Fig. 2(a)]. To test the possible influence of phosphorylation on NCBD binding, a radioisotope-based screen of 51 kinases was performed for their ability to phosphorylate NCBD (see Methods). We focused on the CMGC family,[47] an essential and large group of kinases present in all eukaryotes that includes cyclin-dependent kinases (C), mitogen-activated protein kinases (M), glycogen synthase kinases (G), and CDC-like kinases (C), and which consists primarily of Pro-directed Ser/Thr kinases. The screen identified 12 hits, of which CDK5, CDK1, HIPK2, and p38 were selected as representative examples of the different groups within the CMGC family and for which phosphorylation of NCBD could be confirmed by mass spectrometry. A more detailed analysis of NCBD phosphorylated by these four kinases using reversed-phase (RP)-HPLC and mass spectrometry revealed phosphorylation to

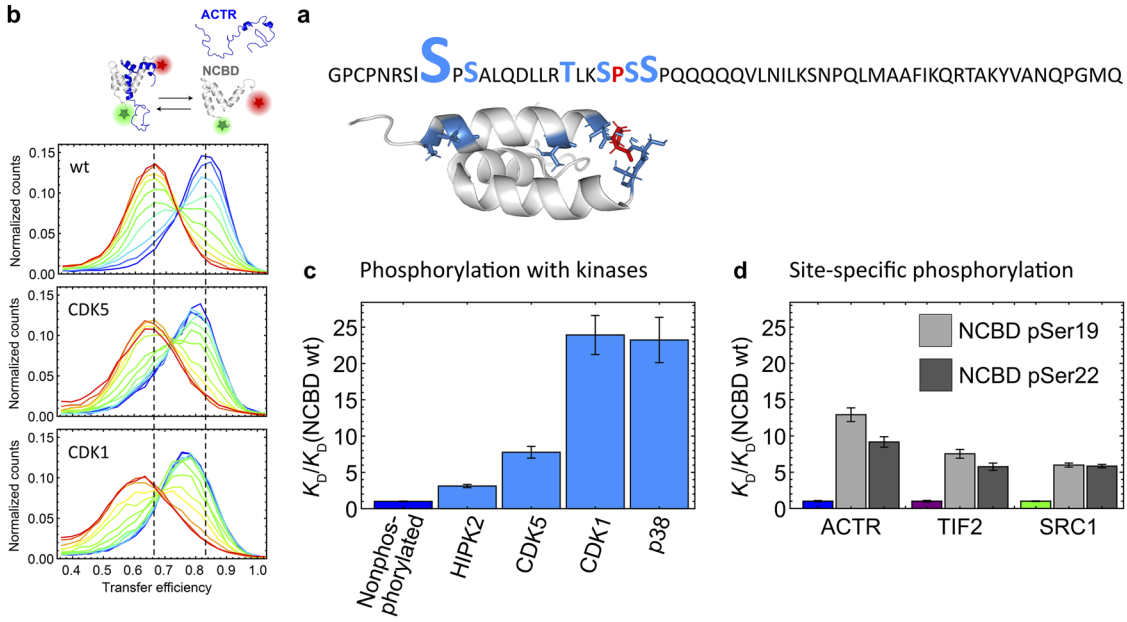

FIG. 2. Effects of NCBD phosphorylation on binding affinity. (a) Sequence and structure of NCBD with the previously reported phosphorylation sites highlighted in blue (PhosphoSitePlus;[48] font size indicates the relative number of reports on this phosphorylation position) and Pro20 indicated in red. (b) Transfer efficiency histograms from free-diffusion single-molecule FRET measurements of double-labeled NCBD (Alexa 488/CF660R) phosphorylated with CDK5 or CDK1 titrated with increasing concentrations of unlabeled ACTR (range: 0–51.2 μM, from blue to red). (c) K_D between ACTR and NCBD upon phosphorylation of NCBD with different kinases relative to unphosphorylated NCBD ("NCBD wt"). (d) Equilibrium dissociation constants of the complexes ACTR-NCBD, TIF2-NCBD, and SRC1-NCBD upon site-specific single-site phosphoserine incorporation (gray) relative to unphosphorylated NCBD (color). Error bars in (c) and (d) indicate the errors of the fits.

occur predominantly at one (CDK5 and HIP2) or two (CDK1 and p38) Ser residues (Fig. S3).

To assess the effect of enzymatic phosphorylation on binding, we performed single-molecule FRET experiments on enzymatically phosphorylated double-labeled NCBD with ACTR [Figs. 2(b), 2(c), and S4, Table S2]. Phosphorylation has clear effects on affinity, with pronounced differences between the kinases. Phosphorylation with CDK1 and p38 increased K_D by more than 20-fold [Figs. 2(b) and 2(c)]; with CDK5 and HIP2, K_D increased much less, indicating that the effect on affinity is amplified with the number of phosphate groups [Figs. 2(c) and S4]. Already based on the net negative charge of ACTR and the net positive charge of NCBD,[37,38,40] we indeed expect phosphorylation of NCBD to reduce the favorable electrostatic contribution to binding, but other effects are likely to contribute as we will show below (see the section titled *Probing the effects of phosphorylation and peptidyl-prolyl cis/trans isomerization with simulations*). An issue with the enzymatically phosphorylated samples is that they exhibit a considerable degree of chemical heterogeneity, especially in terms of the number of phosphate groups, and also by some nonspecific oxidation, a result of the long reaction times required (Fig. S3). Many kinases modify between one and several hundred potential phosphorylation sites *in vivo*, a process that requires complex regulatory mechanisms.[14,15,49] Attaining specific and homogeneous phosphorylation *in vitro* is thus usually difficult, which complicates quantitative analysis.

To achieve specific single-site phosphorylation and enable us to investigate the effects of such modifications on the complexes of NCBD with different binding partners, we thus used NCBD produced by solid-phase peptide synthesis, with phosphoserine (pSer) incorporated at two positions, Ser19 or Ser22; both are in the vicinity of Pro20, which has previously been shown to influence the interaction between NCBD and ACTR by peptidyl-prolyl *cis/trans* isomerization, and both precede a Pro residue and thus form a Ser–Pro motif, a common target for kinases[41–44] [Fig. 2(a)]. The resulting sequences for these site-specifically phosphorylated variants are slightly different from the recombinantly produced proteins, and in these measurements, the NCoAs carry the two negatively charged fluorophores (see Table S1 for sequences), which can affect the absolute affinities, but since we compare identical constructs with and without phosphorylation, the relative changes are expected to be robust. Site-specific phosphorylation of NCBD causes a decrease in affinity for all three NCoAs [Fig. 2(d)], with K_D changes in a similar range as observed upon enzymatic phosphorylation of NCBD and binding to ACTR [Fig. 2(c)]. In summary, phosphorylation of NCBD at both Ser19 and Ser22 destabilizes the complex for all three binding partners, but with differential effects on the different binding partners. Phosphorylation may thus be a way of differentially regulating the interactions of NCBD with closely related binding partners.

Peptidyl-prolyl *cis/trans* isomerization modulates the interaction of NCBD with its binding partners

We recently observed the spontaneous switching of NCBD between two kinetic binding regimes with an eightfold difference in affinity to ACTR.[37] We identified the peptidyl-prolyl *cis/trans* isomerization of Pro20 in NCBD as the dominant source of this kinetic heterogeneity and assigned it to two conformational states ($NCBD_{P20,trans}$ and $NCBD_{P20,cis}$) that interconvert slowly and differ in their kinetics of binding to ACTR [Fig. 3(a)]. To probe the effect of this allosteric process on the binding of NCBD to the different NCoAs, we investigated the kinetics with single-molecule FRET between surface-immobilized molecules and their binding partners in free solution (Fig. 3), which allows timescales from microseconds to minutes to be probed.[37,38,50–53]

We labeled biotinylated NCBD with Cy3B as the donor fluorophore and immobilized it via Avidin on a biotinylated, polyethylene glycol-(PEG-)passivated glass surface [Fig. 3(a)]. Fluorescence from a single NCBD molecule was recorded by confocal single-photon counting. Binding and dissociation were monitored by changes in FRET upon binding to acceptor-labeled molecules present freely diffusing in solution: The time traces exhibit anticorrelated jumps of donor (green) and acceptor emission (red), indicating transitions between the unbound state (high donor counts) and bound state [high acceptor counts, Fig. 3(b)]. In addition to rapid association and dissociation events on the millisecond timescale, we observed within the trajectories of single NCBD molecules two kinetic regimes that interconvert on a timescale of tens of seconds: a high-affinity regime [Fig. 3(b), purple shading], with more frequent and longer binding events than in the low-affinity regime (light green shading). Based on mutation studies, NMR spectroscopy, and molecular dynamics (MD) simulations, we previously assigned the high-affinity regime for the interaction with ACTR to a conformation of NCBD with Pro20 in the *trans* configuration ($NCBD_{P20,trans}$), and the low-affinity regime to NCBD with Pro20 in the *cis* configuration ($NCBD_{P20,cis}$).[37]

Analogous to the procedure described in Zosel *et al.*,[37] we used a hidden Markov model (HMM) based on the kinetic scheme in Fig. 3(a) to quantify the rate coefficients from the time traces by likelihood maximization (MLH) (Table S3). As an alternative analysis approach, we obtained dwell-time distributions of the bound and unbound states with the Viterbi algorithm [Fig. 3(c), see Methods for details]. In agreement with our previous results,[37] the overall dwell-time distribution of the bound state for ACTR decays biexponentially, reflecting the different dissociation rate coefficients associated with the two kinetic regimes. A useful way of visualizing the two regimes is to split the time traces into shorter segments of 4 s and plotting the mean dwell times per segment of the unbound against the bound state ($\langle\tau_{off}\rangle$ vs $\langle\tau_{on}\rangle$) in a 2D histogram [insets in Fig. 3(c)]. For NCBD containing Pro20, the two populations cluster around the rate coefficients from the biexponential dwell-time distributions. This observation is confirmed by separating the segments corresponding to the two kinetic regimes directly in the trajectories and overlaying the resulting 2D histograms [light green and purple dotted lines in insets of Fig. 3(c)]. The kinetic heterogeneity in the dissociation kinetics of ACTR and NCBD is eliminated if Pro20 is replaced by Ala: The homogeneous binding behavior visible in the time trace results in a single population in the 2D dwell-time histogram and a single-exponential dwell-time distribution with a higher decay rate close to that of the *cis* state [Figs. 3(c) and 3(d)]. Although NCBD contains four helix-terminating prolines, only Pro20 affects the switching between the two kinetic regimes observed with ACTR binding to NCBD.[37]

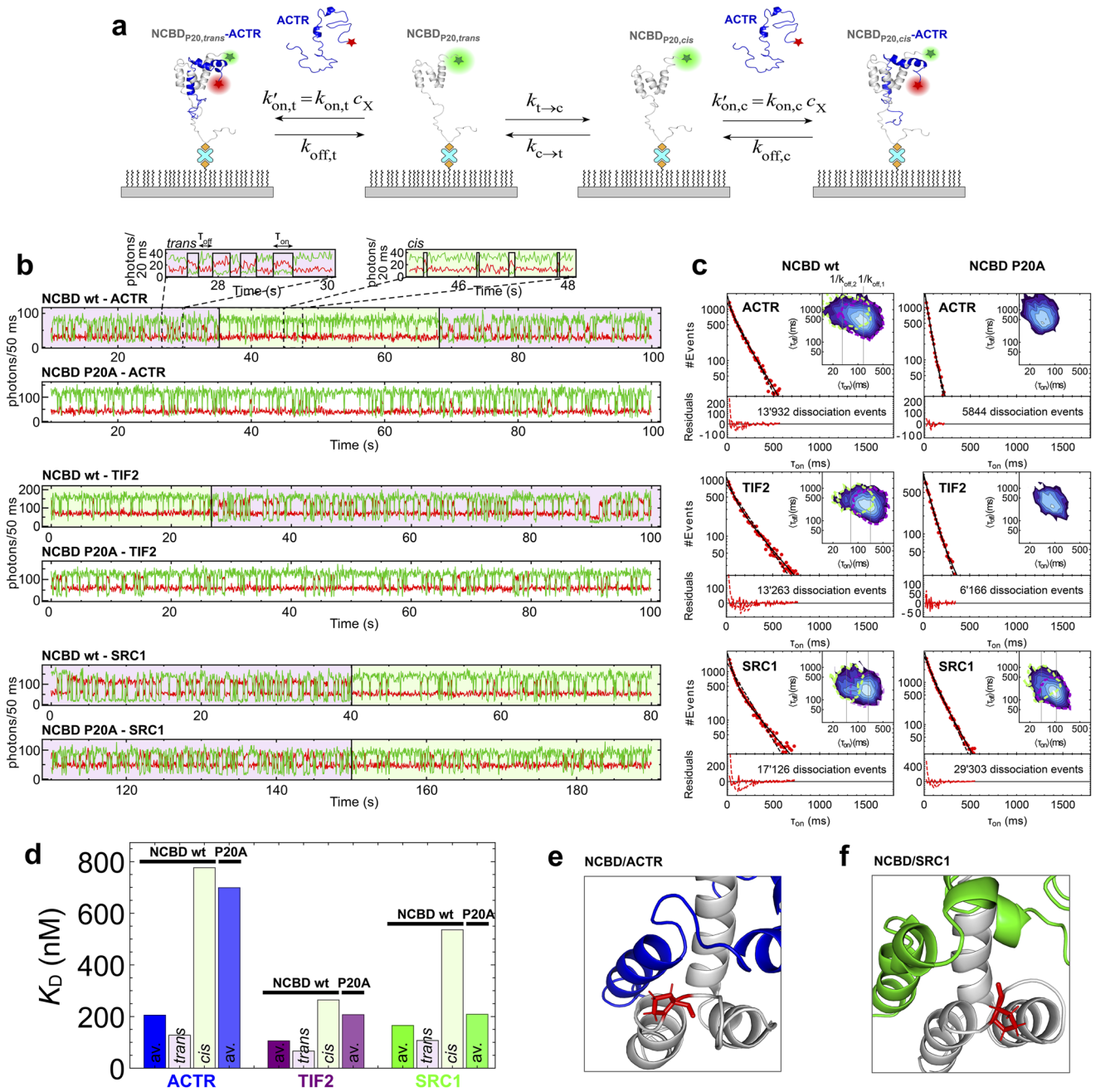

FIG. 3. Peptidyl-prolyl *cis/trans* isomerization causes kinetic heterogeneity in the binding of NCBD to its interaction partners. (a) Schematic representation of the experiment with immobilized NCBD (gray) labeled with Cy3B and binding partner (in this case ACTR, blue) labeled with CF660R. (b) Representative time traces for the binding to ACTR, TIF2, and SRC1 showing time-binned numbers of donor (green) and acceptor photons (red) from confocal measurements. Binding and dissociation events lead to anticorrelated changes of the photon rates. Two kinetic regimes due to Pro isomerization are highlighted: NCBD$_{P20,trans}$ (purple shading) and NCBD$_{P20,cis}$ (green shading). The Viterbi algorithm was used to identify state trajectories from which dwell times of the bound (τ_{on}) and unbound (τ_{off}) states were obtained. (c) Corresponding dwell-time histograms of the bound state of NCBD wt (left) and NCBD P20A (right) fitted with single- (dashed lines) and double-exponential decays (solid lines), with residuals below each panel. Insets show 2D dwell-time histograms of the mean dwell times in the bound ($\langle\tau_{on}\rangle$) and unbound states ($\langle\tau_{off}\rangle$) determined from 4 s segments of the recorded time traces. The inverse values of the dissociation rates ($\langle\tau_{on}\rangle = 1/k_{off}$) are indicated by vertical lines. For variants showing biexponential dwell-time distributions, the two kinetic regimes were separated (see Methods) and the 2D dwell-time histogram overlaid in light green for the *cis* and in purple for the *trans* state. (d) Equilibrium dissociation constants, K_D, for the different binding partners, for NCBD wt on average (av.; based on analysis with a two-state model), separately for *trans* and *cis*, and for NCBD P20A on average (av.). All values provided in Table S3. (e) and (f) Close-ups of the region around NCBD Pro20 (red) in complex with ACTR (e) and SRC1 (f) (PDB 1KBH[20] and 2C52[26]).

Based on this analysis, we addressed the question of whether isomerization of Pro20 in NCBD has a similar effect on its interaction with the other binding partners. Indeed, both for TIF2 and SRC1, we also observe slowly interconverting kinetic regimes [Fig. 3(b)], biexponential dwell-time distributions for dissociation, and two kinetic populations in the 2D histograms (Fig. c, d), reflecting conformational heterogeneity in NCBD. Replacing Pro20 in NCBD by Ala leads to kinetically more homogeneous trajectories [Fig. 3(b)], faster dissociation, and reduced biexponentiality for TIF2 [Fig. 3(c)], similar to ACTR. For SRC1, however, the impact of replacing Pro20 is less pronounced, and more kinetic heterogeneity remains, indicating contributions besides Pro20, which is plausible in view of the structural differences between ACTR and SRC1 bound to NCBD[20,26] [Figs. 3(e) and 3(f); see Table S3 for all resulting parameters] and in line with the small effect of the P20A exchange on K_D [Fig. 3(d)]. To test for possible effects of the immobilization of NCBD on kinetic heterogeneity, we also performed experiments where freely diffusing NCBD binds to immobilized NCoAs (Fig. S6). In this case, we do not expect to observe long-lived heterogeneity in the trajectories,[37] but the presence of NCBD subpopulations with different dissociation rates results in multiexponential dwell-time distributions. The results confirm our findings with immobilized NCBD. In summary, peptidyl-prolyl *cis*/*trans* isomerization of Pro20 does modulate the interaction of NCBD with all three NCoAs, and the binding partners are affected to different extents.

Experimental assessment of coupling between NCBD phosphorylation and the *cis/trans* equilibrium of Pro20

Our results show a clear influence of phosphorylation on the affinity of NCBD to its binding partners (Fig. 2); they also indicate an important role of the *cis/trans* equilibrium of Pro20 in NCBD for the interaction with ACTR and TIF2 (Fig. 3). Since the phosphorylation of Ser residues can alter the *cis/trans* equilibrium of neighboring Pro residues,[54,55] the two effects may be allosterically coupled. To test this hypothesis, we again take advantage of resolving the kinetic heterogeneity caused by peptidyl-prolyl isomerization in single-molecule experiments and probe the effect of NCBD phosphorylation on its interaction with ACTR and TIF2. From the MLH analysis of measurements where NCBD is surface-immobilized, we can estimate the effect of phosphorylation on all kinetic parameters of the model [Fig. 3(a)], including the *cis*/*trans* isomer-specific rate constants, which also enables us to assess the potential thermodynamic coupling between phosphorylation and *cis*/*trans* isomerization (see Methods for details).

Phosphorylation of NCBD at Ser19 and Ser22 accelerates dissociation both for ACTR and TIF2 two- to fivefold, but in all cases, the kinetic stability of the *trans* complex remains greater than that of the *cis* complex [Fig. 4(a) and Table S4]. For the association rate coefficients [Fig. 4(b)], the effects of phosphorylation are less pronounced, with reductions by about a factor of

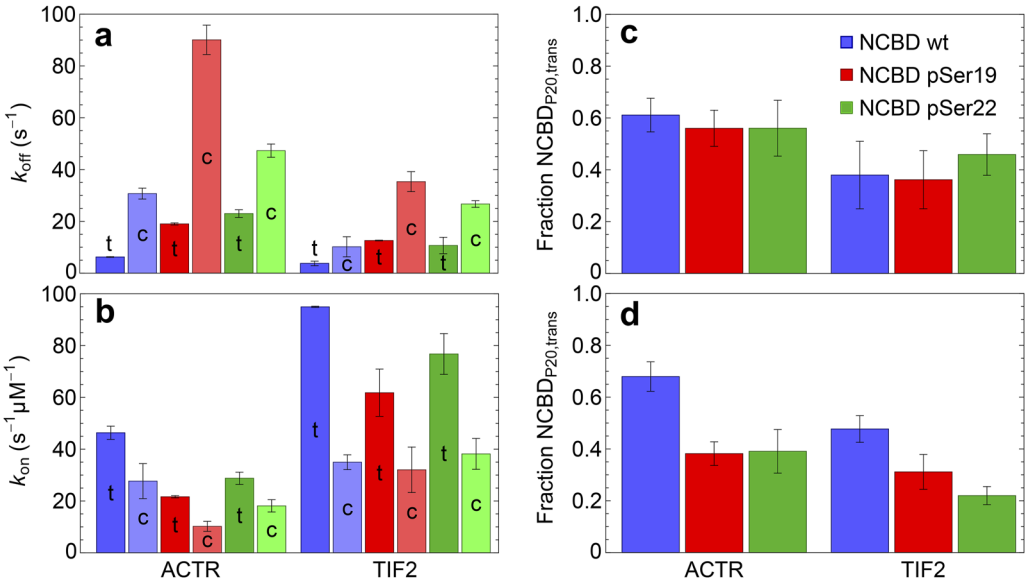

FIG. 4. The effect of NCBD phosphorylation on binding kinetics and the *cis/trans* equilibrium of Pro20. (a)–(c) Kinetic model parameters obtained from the MLH analysis according to the four-state model [Fig. 2(a)] of photon time traces measured from donor-labeled surface-immobilized NCBD observed with acceptor-labeled ACTR or TIF2 binding and unbinding. Compared are in (a) the parameters $k_{off,c/t}$ and in (b) $k_{on,c/t}$ for the *cis* (c) and *trans* (t) subpopulations for unphosphorylated NCBD (blue), pSer19 (red), and pSer22 (green) variants. The association rate constants were obtained from $k_{on,c/t} = k'_{on,c/t}/c_X$, where c_X is the concentration of binding partner *X* in solution, ACTR or TIF2. The values of c_X were quantified using fluorescence correlation spectroscopy (FCS, see Methods). Errors represent the standard deviation estimated from at least two independent datasets. (c) Fraction of NCBD with Pro20 in the *trans* conformation calculated from $k_{c\to t}/(k_{c\to t} + k_{t\to c})$. (d) This fraction can alternatively be quantified from a combined analysis with additional datasets of time traces recorded on surface-immobilized donor-labeled NCoAs and acceptor-labeled NCBD in solution (see Methods). All values provided in Table S4.

two in ACTR for both *cis* and *trans*, and even smaller changes in TIF2, where we observe only slightly decelerated association in the *trans* state. Overall, the reduced affinity caused by phosphorylation [Fig. 3(d)] is dominated by changes in dissociation rates. The resulting equilibrium fractions of NCBD molecules in the *cis* and *trans* states, however, do not yield a significant difference between phosphorylated and unphosphorylated NCBD [Fig. 4(c)].

Since the uncertainties for the individual isomerization rates $k_{c\to t}$ and $k_{t\to c}$ and the resulting equilibrium fractions are relatively large owing to the rare occurrence of *cis*–*trans* transitions in the time traces, we also estimated the isomerization equilibrium constant from the combined analysis of measurements with either NCBD or the NCoAs immobilized, where the influence of *cis*/*trans* isomerization results in deviations of single-exponential behavior in the dwell-time distributions[61] (see Methods for details). Here, we find that Pro20 is on average ~68% in *trans* for unphosphorylated NCBD binding to ACTR [Fig. 4(d)]; phosphorylation of Ser19 or Ser22 decreases this fraction to ~36 or ~37%, respectively. With TIF2 as a binding partner, we obtain a similar drop from ~49% in *trans* for unphosphorylated NCBD to ~30% for NCBD-pSer19

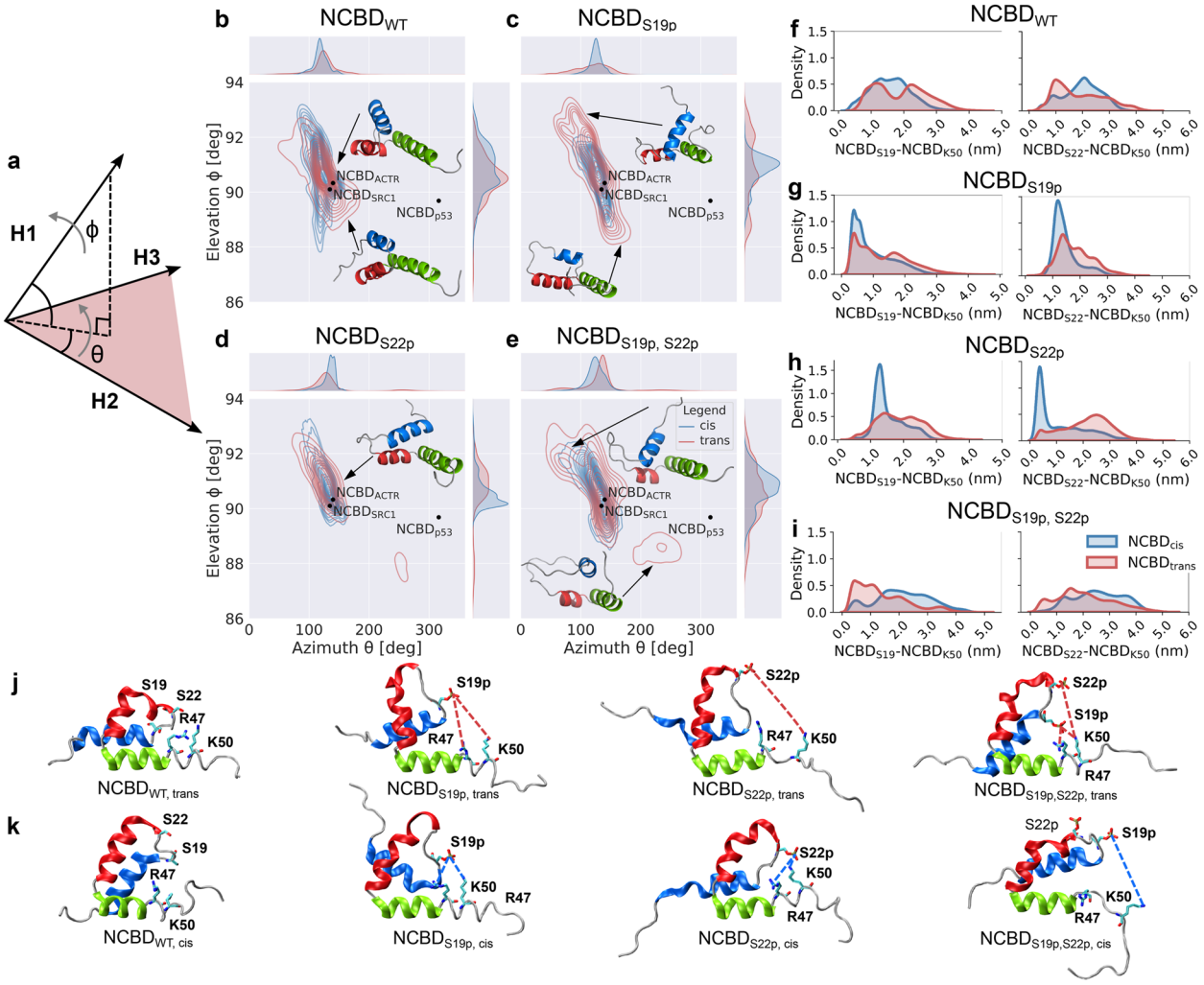

FIG. 5. Effects of phosphorylation on unbound NCBD from MD simulations. (a) Schematic representation of the degrees of freedom characterizing the arrangement of the NCBD helices. (b)–(e) Two-dimensional kernel density estimations of the angles ϕ and θ defining the arrangement of NCBD helices and sampled in the MD simulations (Pro20 in *cis*: blue; *trans*: red). The projected angular distributions are reported alongside the graphs. The black points show the values of the ϕ and θ found in the different experimentally determined structures of NCBD, in complex with ACTR (PDB code: 1KBH[20]), SRC1 (PDB code: 2C52[52]), or p53 (PDB code: 2L14[28]). Insets to the graphs show the most represented conformations obtained from an RMSD-based clustering analysis of the collected trajectories (see Methods for details). Helices 1, 2, and 3 of NCBD are colored blue, red, and green, respectively, while loops connecting the helices are colored gray. (f)–(i) Probability density functions of distances between Ser19 and/or Ser22 and Lys50 for the *trans* (red) and *cis* (blue) ensembles, for NCBD either unphosphorylated (f), phosphorylated on Ser19 (g), phosphorylated on Ser22 (h) or doubly phosphorylated (i). (j) and (k) Representative conformations of NCBD highlighting the proximity of phosphorylated sites and the positively charged region featuring Lys50 and Arg47 (all distances between residues are reported in Fig. S7).

and ~23% for NCBD-pSer22. Although the uncertainties are substantial, these results suggest that phosphorylation of NCBD slightly reduces the *trans* population of Pro20 in both cases. Ideally, we expect the *cis*/*trans* equilibrium for unbound NCBD to be independent of the binding partner. The deviation in absolute values for ACTR and TIF (Tables S3 and S4) might thus originate from slight differences depending on which interaction partner is immobilized; the relative change in *cis*/*trans* equilibrium, however, is observed in both cases and may thus be more reliable. Nevertheless, based on the two different types of analysis, we cannot unequivocally decide whether phosphorylation has a significant effect of the *cis*/*trans* equilibrium, but if it is present, it is moderate in magnitude, with an energetic contribution of less than k_BT [Figs. 4(c) and 4(d)].

In summary, we observe that phosphorylation of NCBD reduces the affinity to its binding partners, with an effect that depends both on the binding partner, the number of phosphate groups, and the phosphorylation site. We also find that peptidyl-prolyl *cis*/*trans* isomerization modulates the binding of NCBD to all the NCoAs investigated here, but to different extents. The linkage between these two effects is at most moderate.

Probing the effects of phosphorylation and peptidyl-prolyl *cis*/*trans* isomerization with simulations

To identify the structural origins and allosteric mechanisms of the experimental effects we observed, we turned to molecular dynamics (MD) simulations. We simulated NCBD alone with Pro20 either in the *trans* or *cis* isomeric state and the ACTR-NBCD complex with Pro20 in the *trans* state, with NCBD either unphosphorylated or phosphorylated at Ser19 and/or Ser22 (Fig. 5). Because of the low rate of *cis*/*trans* isomerization, spontaneous interconversion between *cis* and *trans* was not observed during the simulations, so we used well-tempered metadynamics[56] to obtain starting conformations for the *cis* isomer of NCBD, as previously reported for the exploration of *cis*–*trans* prolyl-isomerization of unphosphorylated NCBD in complex with ACTR.[37] We first analyzed the effect of phosphorylation on free NCBD (Fig. 5). In the unbound state, NCBD exhibits a characteristic arrangement of its three α-helices,[51] which can be described by two degrees of freedom [Fig. 5(a)]: (1) the angle ϕ of helix 1 with respect to the helix 2/helix 3 plane and (2) the azimuth angle θ. These two degrees of freedom reflect the conformation of the loop connecting helices 1 and 2, which contains

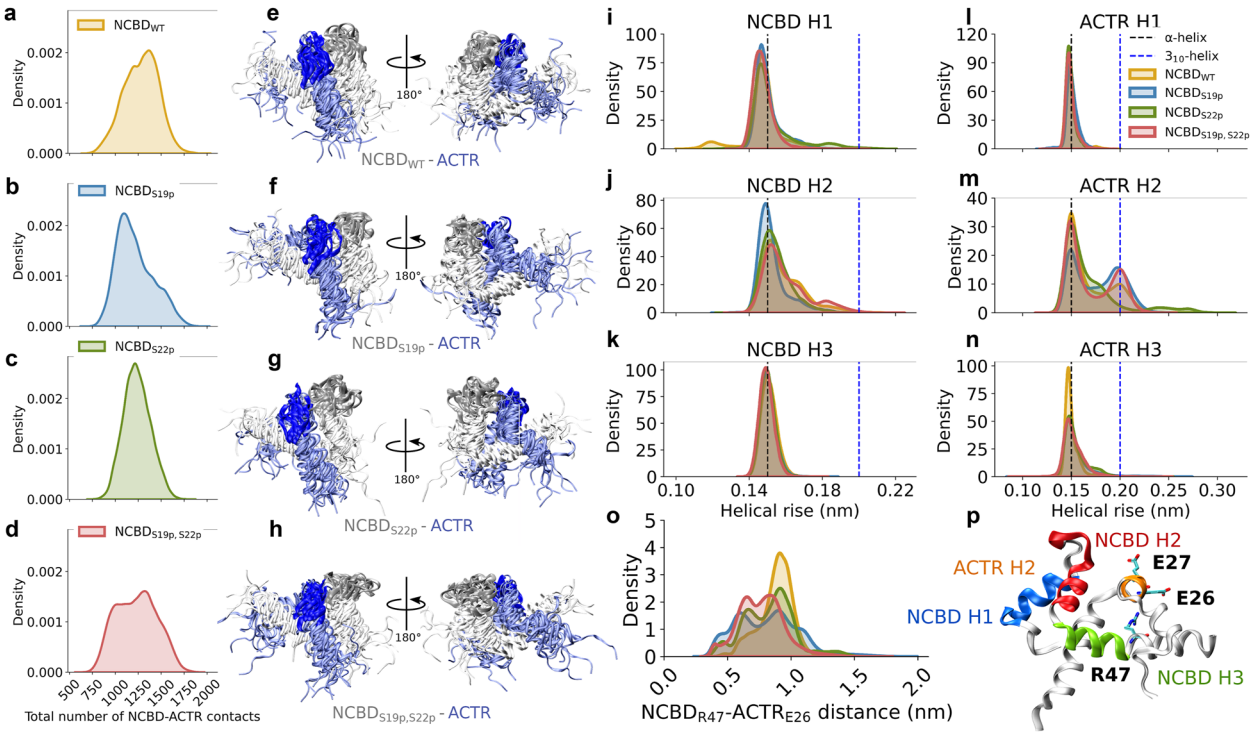

FIG. 6. Effects of phosphorylation on the ACTR-NCBD complex from MD simulations. (a)–(d) Probability density functions of the number of contacts formed between NCBD and ACTR when NCBD is either unphosphorylated (a), phosphorylated on Ser19 (b), phosphorylated on Ser22 (c), or doubly phosphorylated (d). (e)–(h) Ensembles of the NCBD-ACTR complex for NCBD with different phosphorylation states [as in panels (a) to (c)]. Ten conformations sampled in each of the collected ensembles are shown. NCBD is shown in white, except for the Lys18-Pro23 loop, which is shown in dark gray. ACTR is shown in light blue, with the exception of its Thr20-Thr23 loop, shown in dark blue. (i)–(n) Helical rise per residue calculated for each helix in the NCBD-ACTR complex. Ideal values for α-helices and 3_{10}-helices are 0.15 and 0.20 nm, respectively, and are indicated by dashed lines. (o) Distance distribution between Arg47 in NCBD and Glu26 in ACTR and (p) representative structure of the NCBD-ACTR complex to illustrate the close proximity of these two residues.

Pro20, Ser19, and Ser22, and is thus affected by phosphorylation and peptidyl-prolyl *cis/trans* isomerization.

Since only a small number of hydrophobic residues stabilize this arrangement of helices,[51] substantial dynamics are present and entail a broad distribution of angles, especially for ϕ. There is a detectable difference in the angular distributions between the ensembles for the *trans* and *cis* isomers of Pro20 [Figs. 5(b)–5(e)] and the corresponding intramolecular distances [Figs. 5(f)–5(i) and Fig. S1]. Phosphorylation of Ser19 and Ser22 also affects the NCBD ensemble [Figs. 5(c)–5(e) and 5(g)–5(i)]. One important contribution to these changes is likely to be the electrostatic attraction between the phosphate groups and positively charged residues. Such intramolecular salt bridges would be expected to stabilize the unbound state of NCBD and may thus contribute to the reduced affinity and association rate to binding partners we observed experimentally upon phosphorylation [Figs. 2(c), 2(d), and 4(b)]. Indeed, the less binding-competent Pro20 *cis* conformer exhibits a larger population of salt bridges between phosphorylated Ser19 and/or Ser22 and Lys50 in helix 3 of NCBD [Figs. 5(f)–5(k)]. The network of salt bridges within NCBD depends on the phosphorylation state (Fig. S7), with double phosphorylation enhancing the formation of salt bridges between phosphorylated Ser19/Ser22 and positively charged residues on helix 3 [Figs. 5(j), 5(k), and S7]. Salt-bridge formation is further corroborated by the shift of the total electrostatic energy in NCBD to lower (more favorable) values with an increasing number of phosphorylated serine residues [Fig. S7(m)].

The simulations reveal not only effects of phosphorylation on unbound NCBD but also on its complex with ACTR (Fig. 6). Although the overall arrangement of NCBD and ACTR in the complex remains similar both with single- and double-phosphorylated NCBD [Figs. 6(e)–6(h)], the distribution of the number of contacts is shifted to lower values [Figs. 6(a)–6(d)] when NCBD is phosphorylated, suggesting that the complex is destabilized by phosphorylation. This finding is in line with the reduced stability of the complex observed experimentally [Figs. 2(c) and 2(d)] and may contribute to the increased dissociation rate [Fig. 4(a)]. Correspondingly, conformational changes and increased dynamics are detectable in the complex upon phosphorylation, especially in the NCBD loop containing Pro20 [Figs. 6(e)–6(h) and Table S5], where most of the shift in root-mean-square fluctuations concentrates (Fig. S8). This is likely to be driven by electrostatic repulsion between phosphorylated Ser19 and/or Ser22, which are in close proximity with ACTR Asp21 (Fig. S9). Notably, phosphorylation at Ser19 and/or Ser22 not only affects the local loop arrangement but also the conformations in the complex as a whole. An example of such allosteric effects is illustrated in Figs. 6(i)–6(n): Phosphorylation can affect the structure of helix 2 in ACTR, as reflected by changes in helical rise that correspond to the population of a 3–10 helix, together with increased secondary structure (Fig. S10). The likely origin of these conformational changes is again electrostatic in nature. Owing to the close proximity to Ser19 and Ser22 in NCBD, the negatively charged stretch of residues from Glu26 to Asp29 in ACTR is driven into closer proximity with a patch of positively charged residues in NCBD (Lys 45, Arg47, Lys50) upon phosphorylation of the Ser residues [Figs. 6(o) and S11]. The correlation of these changes with the altered helical conformation of ACTR helix 2 suggests that such networks of salt bridges can lead to long-range conformational effects in the complex that are likely to affect its stability.

DISCUSSION

Since many IDPs are involved in cellular regulation networks, identifying the underlying molecular mechanisms is an important challenge.[7] A central regulatory mechanism is posttranslational phosphorylation,[14,15,57] and NCBD is known to be phosphorylated *in vivo*.[41–44] Based on a large-scale screen of 51 kinases, we identified four that phosphorylate NCBD predominantly at one or two Serine residues. The resulting up to 20-fold decrease in affinity to ACTR is greater if two rather than one Ser is modified, showing that phosphorylation can indeed have a pronounced and tunable effect on complex formation. However, enzymatic phosphorylation typically yields polydisperse samples, which limits detailed site-specific investigations. We thus also introduced single phosphoserine residues site-specifically by chemical peptide synthesis and found similar changes in K_D by up to about an order of magnitude for the NCBD-ACTR complex, and slightly less for SRC1 and TIF2 [Fig. 3(d)]. An obvious reason for this effect is that the binding of NCBD with its positive net charge to the three net-negatively charged NCoAs is electrostatically favored, like many interactions involving IDPs.[9,58] This electrostatic driving force has previously been shown by the sensitivity of the kinetics and equilibrium complex stability to changes in ionic strength.[55] The reduction in net charge of NCBD by phosphorylation is thus expected to reduce the affinity, as we observe. Conversely—but consistently—phosphorylation of the negatively charged p53TAD has been observed to increase its affinity to NCBD.[59] However, the MD simulations indicate that simple electrostatic interactions are not the only contribution; instead, phosphorylation alters both the structural ensemble of free NCBD and the number of contacts and the flexibility of the complex, corresponding to allosteric effects.[17,60]

We recently observed another effect that modulates the affinity and interaction kinetics of the coupled folding and binding to its partner ACTR: peptidyl-prolyl-*cis/trans* isomerization of Pro20 in NCBD acts as a conformational switch.[37] To assess the generality of this effect, we investigated here several other binding partners of NCBD, especially the other two NCoAs SRC1 and TIF2. Moreover, we probed the influence of phosphorylation on binding equilibria and kinetics. Interestingly, the results for SRC1 and TIF2 are quite different. We find that Pro20 isomerization in NCBD is a key factor modulating the interaction with TIF2. As for ACTR, *cis/trans* isomerization of this residue leads to two complexes with different stability and interaction kinetics, with slower dissociation in the predominant *trans* state. Exchanging Pro20 to Ala largely eliminates this kinetic heterogeneity. In contrast, SRC1 binding is influenced not only by *cis/trans* isomerization of NCBD Pro20. Rather, our experiments [Fig. 3(d)] suggest the presence of two kinetically distinguishable NCBD populations even in the absence of Pro20. The influence of isomerization of other proline residues on the complex is plausible, given the differences in the structures of NCBD-ACTR and NCBD-SRC1 [Figs. 1(a), 3(e), and 3(f)]. These observations indicate an elaborate set of coupled binding equilibria, where the affinities to NCBD differ not only by the interaction partner *per se* [Fig. 1(c)] but also by the *cis/trans* isomerization state of specific Pro residues in NCBD. Our observations on the effects of phosphorylation on binding on the one hand and of peptidyl-prolyl *cis/trans* isomerization on the other raise the question of whether the two processes might be allosterically coupled, especially since phosphorylation of Ser residues directly preceding Pro has been reported

to shift the equilibrium of Pro toward the *cis* isomer.[54,55] However, based on our experimental results, if the effect is present in NCBD, it is weak, with an upper bound to the effect on the complex stability of ~1 k_BT [Figs. 4(c) and 4(d)].

Altogether, our results suggest multiple layers of allosteric regulation in the folding-coupled binding interactions of NCBD. First, the affinities to its different binding partners, in which NCBD assumes slightly to very different conformations,[20,21,26,28,45] span more than two orders of magnitude[20,40,46] (Figs. 1 and S1). The different complexes are thus likely to be populated and to exert their maximal effects at very different protein concentrations in the cell. Second, both phosphorylation and peptidyl-prolyl *cis/trans* isomerization in NCBD affect these interactions and the underlying conformational ensemble to different extents, which enables differential regulation. Third, all binding partners present in the cell will compete for NCBD, resulting in a delicate network of linked equilibria that can be fine-tuned by changes in protein concentrations and posttranslational modifications acting via allosteric effects. Such multilayered allosteric regulation is likely to be part of the tissue- and development-specific roles of NCoAs, which are associated with various forms of cancer.[61,62] Additional mechanisms will of course be involved within the multidomain context of these proteins. For instance, a recent report using cryo-electron microscopy suggests the presence of a quaternary complex involving DNA, estrogen, and two ACTR molecules binding to CBP simultaneously.[63] Therefore, this complex is likely to also involve interactions of ACTR with other CBP domains, including allosteric effects. Finally, recent evidence indicates that p300 can undergo phase separation with some transcription factors,[64] which may add yet another level of regulation. The quantitative characterization of such interactions will be essential for truly understanding cellular regulation.

Our work also illustrates some of the key challenges in quantitatively elucidating regulatory interaction networks. First, even for simple kinetic schemes, such as the binding between two interaction partners and isomerization of a single Pro residue [Fig. 3(a)], the resulting kinetics can be nontrivial to analyze and model accurately, although single-molecule spectroscopy can be useful for complementing ensemble-based approaches and resolving kinetic heterogeneity.[37] Second, such contributions can be coupled: the interaction of a hub protein with multiple binding partners; peptidyl-prolyl *cis/trans* isomerization; and the effect of PTMs. Third, as a result of this multilayered allosteric regulation, we are facing a combinatorial explosion: Already with a handful of binding partners, the potential influence of isomerization of several Pro residues, and the dozens of PTMs known for NCBD and its binding partners, hundreds of combinations or more need to be accounted for. Fourth, even though some of these contributions can alter affinities and kinetics by orders of magnitude, some effects are only in the range of thermal energy, k_BT. Nevertheless, even such factors of two to three in interaction kinetics or equilibria may have important effects on cellular regulation and are in the regime often observed for effects from macromolecular crowding.[39,65,66] Some of these contributions may compensate each other and lead to more robust regulation.[67] Addressing these challenges for complex regulatory networks and the underlying allosteric effects in the cell will be a daunting task and may require the integration of quantitative biophysical investigations and modeling with other approaches, such as high-throughput interaction studies, cybernetics/systems biology, and experiments in live cells.

METHODS

Protein expression

All protein sequences are summarized in Fig. S1. The NCBD-binding domains of the three human NCoAs (ACTR: UniProt Q9Y6Q9 (1018–1088), TIF2: UniProt Q15596 (1049–1116), and SRC1: UniProt Q15788 (902–971)) as well as of p53TAD (UniProt P04637, 13–61) and of E1A (UniProt P03259, 35–81) were subcloned into a pAT222-pD vector (gift of J. Schöppe and A. Plückthun[68]). The constructs have an N-terminal Avi-tag that is cleavable by HRV 3C protease and a C-terminal Cys followed by a thrombin-cleavable His_6-tag. Compared to the naturally occurring sequence of TIF2 and SRC1, the naturally occurring Cys residues near the N-terminus were replaced by Ser using site-directed mutagenesis to avoid interference with labeling (cf. Fig. S2). For all three NCoAs, terminal double-Cys variants were obtained by site-directed mutagenesis. The pAT222-pD plasmids were co-transformed with the pBirAcm (Avidity, Aurora CO) for *in vivo* biotinylation of Lys12 of the Avi-tag for expression in *E. coli* BL21(DE3) Tuner cells as described before.[37] The harvested cells were lysed either by sonication or by addition of 6M GdmCl; the His_6-tagged protein was enriched via Ni-IDA IMAC (ABT); and the His_6-tag was cleaved off by thrombin (Serva). To remove the cleaved tags as well as unbiotinylated protein, reversed-phase HPLC (RP-HPLC) was carried out in a H_2O/0.1%TFA–acetonitrile gradient (typically ranging from 40% to 70% acetonitrile) on a C18 column (Reprosil Gold 200, Dr. Maisch). For the Avi-IDP constructs, this step was followed directly by the thrombin cleavage, whereas for the other IDP constructs, the Avi-tag was first cleaved off by HRV 3C protease. RP-HPLC-purified protein was lyophilized and stored at −80 °C until further use.

Avi-NCBD constructs are based on the construct previously described[38] but lacking the P20/23A exchanges, and the P20A mutation was generated by site-directed mutagenesis. Expression and purification were carried out as for the Avi-IDPs. NCBD DL and ACTR without Cys were prepared by site-directed mutagenesis of the genes cloned into the pET-47b(+) vector and expressed as described previously.[37] NCBD and NCBD P20A labeled with Biotium CF680were prepared previously.[37]

The synthetic NCBD phosphovariants were obtained by peptide synthesis performed by Biosyntan GmbH (Germany). The N-terminal Avi-tag was shortened compared to the expression variants to enable chemical synthesis. Therefore, the biotin-modified Lys was chosen as the first amino acid; additionally, the two synthesized variants carried either a phosphate on Ser19 or Ser22. Lambda protein phosphatase (NEB) was used for dephosphorylation, and endoproteinase GluC (NEB) for cleaving off the Avi-tag, according to the manufacturer's instructions. By combining these two steps with labeling, the nine variants used for the experiments with site-specific phosphorylation were obtained.

For unlabeled NCBD, TIF2, p53TAD, E1A as well as all Avi-tag-containing proteins, the absorbance at 280 nM was used to quantify the protein concentration on a NanoDrop 2000 spectrophotometer (ThermoFisher). However, ACTR and SRC1 do not contain aromatic residues. For ACTR, the previously determined extinction coefficient at 225 nm was used (ε_{225nm} = 4.22 $(mg/ml)^{-1}$ cm^{-1}).[69]

Since the NCoAs have similar lengths (79 or 78 residues), the concentration of SRC1 was approximated using the extinction coefficient of ACTR. Independent measurements using Ellman's reagent[70] for the concentration determination of Cys residues confirmed the previous estimation.

Protein labeling

The different protein variants and the respective fluorescent labels are summarized in Table S1. For labeling, lyophilized protein was dissolved in 50 mM sodium phosphate, pH 7 to a concentration of ~100 μM under nitrogen atmosphere. For single-labeled variants, the lyophilized dye was dissolved in dimethylformamide (DMF) to a concentration of ~5 mM, and the protein was labeled at a 1:1.2 molar protein-to-dye ratio for 2–5 h at room temperature. Free dye and unreacted protein were then removed by RP-HPLC and the single-labeled protein lyophilized. For double-labeled variants, the first fluorophore (donor) was added in a ~1:0.8 molar protein-to-dye ratio to minimize the formation of protein modified with two donor dyes. Unreacted dye and protein were removed by RP-HPLC, and the protein was lyophilized. In the second labeling step, the acceptor fluorophore was added at a ~1:1.5 molar protein-to-dye ratio and purified by RP-HPLC followed by lyophilization. The correct masses of the labeled proteins were confirmed by electrospray ionization mass spectrometry (ESI-MS). Examples of Avi-NCBD with and without Pro20 labeled with Cy3B are shown in Fig. S5. The concentrations of fluorescently labeled proteins were quantified based on the extinction coefficients of the dyes provided by the manufacturers.

Enzymatic phosphorylation of NCBD

A phosphorylation screen based on the direct quantification of radiolabeled phosphate from ATP performed by Kinexus Bioinformatics Corporation (Canada) revealed that NCBD is phosphorylated by the following kinases: CDK5, CDK1, HIPK2, and p38. For phosphorylation, double-labeled NCBD at a concentration of 110 μM was mixed with 30–50 nM of the kinases CDK5 (CDK5/p25NCK, ProQuinase), CDK1 (CDK1/CycA2, ProQuinase), HIPK2 (SignalChem), or p38 (p38δ, ProQuinase). The reaction was performed in 50 mM HEPES, pH 7.45, 100 mM NaCl, 5 mM $MgCl_2$ in the presence of 1 mM TCEP, 0.01% Tween 20 (Pierce), and 2 mM adenosine triphosphate for 48 h at 37 °C. The RP-HPLC-purified phosphorylated NCBD was lyophilized and the mass confirmed by ESI-MS.

Single-molecule experiments of freely diffusing molecules

Single-molecule measurements of freely diffusing molecules were carried out on a custom-built confocal instrument with a 488 nm solid-state laser (FCD488-010, JDSU) and an Olympus UplanApo 60 × /1.20W objective. An excitation power of 100 μW (measured at the back aperture of the objective) was used to excite the donor fluorophore (Alexa Fluor 488). Emitted photons were focused onto a 100 μm pinhole and divided into donor and acceptor photons by a dichroic mirror (585DCXR, Chroma Technology). Donor photons were filtered by a longpass filter (ET525/50M, Chroma Technology) before reaching the single-photon avalanche diode (SPAD, MPD 100 ct, Micro Photon Devices). Accordingly, for the acceptor photons, which were filtered either with a QT 650/100 bandpass filter (Semrock, for Alexa Fluor 594) or a LP647RU longpass filter (Semrock, for Biotium CF660R) before reaching the detector (SPCM-AQR-13, PerkinElmer). The data for labeled NCBD binding to ACTR in 1M TMAO [Figs. 1(c) and 1(d)] and the kinase-phosphorylated NCBD interactions were recorded on a MicroTime 200 (PicoQuant, Berlin) in a configuration that was previously described in detail,[69] but with an LP647RU longpass filter (Semrock) used instead of the HQ650/100 bandpass filter (Chroma Technology).

For measurements, the labeled proteins (NCoAs with Alexa Fluor 488/594 or NCBD with Alexa Fluor 488/Biotium CF660R) were used at nominal concentrations of 50 pM (NCoAs) or 200 pM (NCBD) in 50 mM sodium phosphate buffer (pH 7) supplied with 0.01% Tween 20 (Pierce) to prevent surface adhesion of the protein and 140 mM β-mercaptoethanol (Sigma) as a photoprotective agent.[71] Binding experiments with preformed complex [equilibrated for at least 5 min in a Protein LoBind microcentrifuge tube (Eppendorf)] were performed in a small polymer sample chamber (μ-Slide Angiogenesis, ibidi) to minimize both surface adhesion of the positively charged NCBD and sample consumption. Data analysis was performed with Fretica, a custom add-on for Mathematica (Wolfram Research) available at https://schuler.bioc.uzh.ch/programs. Transfer efficiency histograms were calculated as previously described,[72] with a minimum of 100 photons per burst and a maximum interphoton time of <150 μs. Bursts with $E \approx 0$ from proteins lacking an active acceptor fluorophore were not included in the analysis. The transfer efficiency histograms were fit with two Gaussian peak functions for NCoAs labeled with Alexa Fluor 488/594; or with one lognormal peak function for unbound NCBD with Alexa Fluor488/Biotium CF660R and a Gaussian function for its bound form.[73] In a first step, the unbound population in the absence of binding partner was fit and the resulting peak position, width, and asymmetry (for the lognormal function of unbound NCBD) were fixed. Then, the position and width of the bound population were fit as shared parameters globally for each titration, while the amplitudes of both peaks were not shared. Fractions of labeled species in the bound state, f_{bound}, were calculated from the relative peak areas. Affinities were obtained using a binding isotherm to describe the fraction of bound molecules as a function of the concentration c of the unlabeled species, $f_{bound} = c/(K_D + c)$.

Note that for all experiments with SRC1, we removed the naturally occurring Cys residues in the N-terminal disordered tail (Table S1). To test whether this alteration affects the binding affinity, we performed titrations of labeled NCBD with unlabeled wild type SRC1 (Fig. S2). The peak positions of bound NCBD [Figs. S2(a) and S2(c)] as well as the affinities [Fig. S2(d)] do not differ for SRC1 with and without those Cys residues. TIF2 contains only one Cys in the wild type sequence of the N-terminal disordered tail. Based on the results for SRC1, which do not indicate any involvement of the Cys residues in binding to NCBD, we considered the relevance of the Cys in TIF2 for binding to be also negligible and removed it.

The Förster radius of 4.6 nm for the dye pair Alexa Fluor 488 and Biotium CF660R[48] was calculated based on the emission spectrum of Alexa Fluor 488 and the absorption spectrum of CF660R

(with the extinction coefficient of the acceptor according to the manufacturer's specification).[74]

Single-molecule experiments of surface-immobilized molecules

Single-molecule experiments of surface-immobilized molecules were carried out on a MicroTime200 confocal single-molecule instrument (PicoQuant). The sample was excited with a 532 nm continuous-wave laser (LBX-532-50-COL-PP, Oxxius) and a 635 nm pulsed diode laser operated at a repetition rate of 40 MHz (LDH-D-C-635M, PicoQuant). Fluorescence was separated from scattered light by a triple-band mirror (zt405/530/630rpc, Chroma Technology) and a longpass filter (532 LP Edge Basic, Chroma Technology). Fluorescence was collected by an Olympus UplanApo 60×/1.20W objective, passed through a 100 μm pinhole, and split according to wavelength by a dichroic mirror (T 635 LPXR, Chroma Technology). Donor emission was filtered with a 585/65 ET bandpass filter (Chroma Technology) and acceptor emission with a longpass filter (LP647RU, Semrock) before being directed onto SPCM-AQRH-14 single-photon avalanche diodes (Perkin Elmer). For scanning, the objective (UPlanApo 60×/1.20 W, Olympus) was mounted on a piezo stage (P-733.2 and PIFOC, Physik Instrumente GmbH).

Measurement chambers for surface experiments were prepared by binding adhesive silicone hybridization chambers (Secure Seal Hybridization Chambers, Grace Bio-Labs) to PEGylated and covalently biotinylated quartz coverslips (Bio 01, MicroSurfaces Inc.). To minimize fluorescence background, the coverslips were boiled in water/0.1% Tween20 (Sigma) and sonicated for 10 min before binding to the hybridization chambers. For the immobilization of Avi-tagged proteins, a complex between Avidin D (Vector Labs) and the biotinylated protein was preformed at a 12:1 ratio (60 nM:5 nM) in 50 mM sodium phosphate (pH 7) supplemented with 0.01% Tween20. Before binding it to immobilized biotin in the measurement chamber, the complex was diluted 1:190 in the same buffer. The immobilization reaction was monitored by repeated measurements of fluorescent spots on a small surface area (20 × 20 μm^2) with the 532 nm laser at 3 μW (measured at the back aperture of the objective) and stopped as soon as enough molecules were detected (~30–50 per area). The measurement cell was then washed three times with buffer.

Time traces of immobilized single molecules were acquired with the labeled binding partner (CF680R for NCBD, CF660R for the NCoAs) present in nanomolar concentrations in 50 mM sodium phosphate buffer, pH 7, supplemented with 0.01% Tween20 to reduce surface adhesion, and 1% (w/v) glucose, 1 μg/ml glucose oxidase (Sigma), and 2 U/ml catalase (Sigma) were used as an oxygen scavenging system.[75] Furthermore, 1 mM methyl viologen and 1 mM ascorbic acid were included as triplet quenchers.[76] The measurements were performed at 22 °C under argon atmosphere. By scanning a small area (15 × 15 μm^2) with the 532 nm laser at 3 μW (measured at the back aperture of the objective), the positions of immobilized proteins were determined by their fluorescence emission. The laser intensity was reduced to 0.3 μW for the measurement of time traces to reduce the bleaching rate of the fluorophores, and the axial position of the focus was adjusted manually to maximize photon counts. Around 70–200 single-molecule trajectories were acquired until photobleaching, with data collection performed using a custom-developed software written in C++. Single-molecule trajectories were selected for binding and stable photon counts by visual inspection.

To determine the concentrations of binding partner free in solution (either labeled with Biotium CF660R or CF680R), fluorescence correlation spectroscopy (FCS) curves were measured before and after each acquisition of fluorescence trajectories with the 635 nm diode laser (40 MHz). The laser focus was positioned 20 μm above the cover slide, and emission was separated by polarization. The amplitude of the cross correlation of the polarization channels is inversely proportional to the average number of molecules present in the confocal volume, $\langle N \rangle$, and was used to estimate the ligand concentration in solution.[77] To reduce the experimental uncertainty in active ligand concentration, we removed large fluorescence bursts originating from protein aggregates from the recordings, and measurements of CF660R- and CF680R-labeled protein samples of known concentrations were used for calibration. The FCS measurements were fit with a model including translational diffusion and triplet dynamics,

$$G_{AA}(\tau) = 1 + \frac{1}{\langle N \rangle}\left(1 + \frac{\tau}{\tau_D}\right)^{-1}\left(1 + s^2\frac{\tau}{\tau_D}\right)^{-1/2}\left(1 + c_T \exp\left(-\frac{\tau}{\tau_T}\right)\right), \quad (1)$$

where s is the ratio of the lateral to axial radii of the confocal volume and was set to 1/6 based on previous calibration measurements. The correlation time of triplet blinking, τ_T, and its amplitude, c_T, were obtained from the calibration curves and fixed for fitting of the other curves. The translational diffusion time, τ_D, and $\langle N \rangle$ were thus the only free fit parameters.

Analysis of single-molecule time traces

The hidden Markov model (HMM) analysis of binned photon time traces recorded from surface-immobilized single molecules applied here is essentially identical to the one described in Zosel *et al.*[37] As observed before, *cis/trans* isomerization does not change the transfer efficiency of the bound state to within experimental uncertainty.[37] In a first step, we thus assumed a simple kinetic two-state model for NCBD (N) binding to the NCoA (X),

$$N \underset{k_{off}}{\overset{k'_{on}}{\rightleftharpoons}} N - X,$$

with $k'_{on} = k_{on}c_X$. Here, we assume that the observed NCBD molecule is surface-immobilized and that the NCoA is free in solution with bulk concentration c_X. Using a maximum likelihood (MLH) approach,[61,78,79] we obtained for each time trace the mean donor and acceptor photon detection rates in both states and the most likely values for k'_{on} and k_{off}. A time binning of 1 ms was used, and the kinetic scheme was extended to take fluorescence blinking into account, as described previously.[37] The average K_D values reported in Fig. 3(d) were calculated using $K_D = k_{off}c_X/k'_{on}$. The Viterbi algorithm was used to calculate state trajectories, from which dwell-time distributions of the bound state were obtained [Figs. 3(c) and 3(d)] and either fit with a single-exponential ($A \cdot e^{-k_{off}\cdot t}$) or a double-exponential decay ($A_1 \cdot e^{-k_{off,1}\cdot t} + A_2 \cdot e^{-k_{off,2}\cdot t}$) to obtain the corresponding rate coefficients. Since the state detection with the

Viterbi algorithm is not very reliable for short dwell times,[37] we excluded dwell times below 20 ms from the analysis. Based on the bound and unbound states assigned by the Viterbi algorithm, 2D dwell-time histograms (Fig. 2) were constructed by splitting the time traces into 4 s segments and plotting the mean dwell times in the unbound ($\langle\tau_{off}\rangle$) vs bound state ($\langle\tau_{on}\rangle$) for each segment as a contour plot. For comparison, the inverse values of the fit dissociation rate coefficients obtained from the fits to the dwell-time histograms are indicated in the same plots.

For experiments where peptidyl-prolyl *cis/trans* isomerization of NCBD affects the binding kinetics, a two-state model is insufficient. We distinguish two cases: If we monitor the behavior of an individual donor-labeled NCBD molecule N immobilized on the surface, which binds to freely diffusing acceptor-labeled NCoA of type X, the four-state model depicted in Fig. 2(a) applies,[37]

$$X - N_{trans} \underset{k'_{on,t}}{\overset{k_{off,t}}{\rightleftharpoons}} N_{trans} \underset{k_{c\leftarrow t}}{\overset{k_{t\rightarrow c}}{\rightleftharpoons}} N_{cis} \underset{k_{off,c}}{\overset{k'_{on,c}}{\rightleftharpoons}} N_{cis} - X.$$

However, if we monitor the behavior of an individual donor-labeled NCoA molecule, X, immobilized on the surface, which binds to acceptor-labeled NCBD free in solution (N), a three-state model applies,[37]

$$N_{trans} - X \underset{k'_{on2,t}}{\overset{k_{off,t}}{\rightleftharpoons}} X \underset{k_{off,c}}{\overset{k'_{on2,c}}{\rightleftharpoons}} X - N_{cis}.$$

In the first case, we obtain from the MLH analysis (again taking blinking into account[37]) the kinetic parameters $k'_{on,t}$, $k_{off,t}$, $k'_{on,c}$, $k_{off,c}$, $k_{c\rightarrow t}$, and $k_{t\rightarrow c}$; in the second case, we obtain $k'_{on2,t}$, $k_{off,t}$, $k'_{on2,c}$, and $k_{off,c}$. The pseudo-first-order association rate coefficients (primed) are related to the underlying association rate coefficients (unprimed) by $k'_{on,t} = k_{on,t}c_X$, $k'_{on,c} = k_{on,c}c_X$, $k'_{on2,t} = k_{on,t}f_t c_N$, and $k'_{on2,c} = k_{on,c}(1-f_t)c_N$, where c_X is the concentration of the NCoA free in solution; c_N is the concentration of NCBD free in solution; and f_t is the average fraction of NCBD with Pro20 in *trans* (in the absence of binding partners). The uncertainties for $k_{c\rightarrow t}$ and $k_{t\rightarrow c}$ are relatively high owing to the rare occurrence of *cis–trans* transitions in the time traces, but the isomerization equilibrium constant $K_{iso} = k_{c\rightarrow t}/k_{t\rightarrow c}$ is obtained more robustly from the definitions of $k'_{on2,t}$ and $k'_{on2,c}$ as

$$K_{iso} = \frac{f_t}{(1-f_t)} = \frac{k'_{on2,t}}{k'_{on2,c}}\frac{k'_{on,c}}{k'_{on,t}},$$

which thus allows f_t to be determined [Fig. 4(c)]. With the concentrations c_N and c_X from FCS, we obtained the values for $k_{on,c}$ and $k_{on,t}$. The K_D values for *cis* and *trans* reported in Fig. 3(d) were calculated using $k_{off,c}/k_{on,c}$ and $k_{off,t}/k_{on,t}$, respectively, using only data with NCBD immobilized.

Molecular dynamics simulations of NCBD in isolation and in complex with ACTR

Molecular dynamics (MD) simulations of the isolated NCBD and the NCBD-ACTR complex (PDB accession code 1KBH[20]) were performed using GROMACS version 2019.[80,81] The AMBER99disp force field, specifically optimized for both intrinsically disordered and structured proteins,[82] was employed for all simulations. AMBER-compatible parameters for phosphorylated serine were obtained from Homeyer *et al.*[83] Initially, each system was placed in a cubic box after adding hydrogen atoms and solvated with TIP4PD water molecules.[84] Na^+ and Cl^- ions were added to neutralize the net charge and reach a final ionic strength of 165 mM. Each system was then energy-minimized and simulated for a 0.5 μs production MD run. Before the production run, thermodynamic variables, such as temperature and pressure, were normalized in two equilibration steps. A first 500 ps equilibration step was performed in the nVT ensemble with a positional restraint applied on all protein atoms in the three dimensions using a force constant of 1000 kJ mol^{-1} nm^{-1}. In this step, random velocities were assigned to the particles considering the target temperature of 298.15 K, according to the Maxwell–Boltzmann distribution. Temperature was kept constant using a velocity rescaling thermostat,[85] coupling temperature every 0.1 ps, independently for the protein and the rest of the system (water and ions). A second equilibration step was started based on the velocities of the last frame obtained from the previous nVT equilibration and performed while keeping the positional restraints on the protein atoms in the nPT ensemble, coupling both temperature and pressure. While temperature was coupled as in the previous step, pressure was coupled using a Parrinello–Rahman barostat[86] applied isotropically to reach a target pressure of 1.0 bar coupled every 2.0 ps, considering the isothermal compressibility of water (4.5×10^{-5} bar^{-1}). Following the second equilibration step, the production run was performed in the nPT ensemble without positional restraints. nVT, nPT, and production runs were all performed with constraints on all atomic bonds using the LINCS algorithm.[87] van der Waals (vdW) interactions were described with a 12-6 Lennard-Jones potential, electrostatic forces with a Coulomb potential, both with a cutoff of 1.4 nm. For long-range electrostatic interactions beyond the cutoff, forces were computed in reciprocal space using the particle mesh-Ewald (PME) method,[88] with a cubic interpolation on a grid spaced at 0.16 nm.

For all simulations, periodic boundary conditions were applied. The Verlet scheme[89] was used to obtain lists of neighboring particles falling within the adopted cutoff. The last conformer obtained from this equilibration was used to start well-tempered metadynamics[56] in order to obtain equilibrated *trans* and *cis* conformations of isolated NCBD Pro20. To sample peptidyl-prolyl isomerization, the dihedral angle formed by the atoms $^{pS19}C_\alpha$–^{pS19}C–^{P20}N–$^{P20}C_\alpha$ (ω-angle) was used as the collective variable and biased by adding Gaussian functions of energy with a height of 0.2 kJ mol^{-1} and a width of 0.2 radians, using as bias factor a value of 6, and temperature at 298.15 K. Well-tempered metadynamics simulations[90] were carried out using GROMACS patched with the Plumed plugin version 2.35.[91] From the metadynamics run, two conformations of wild type and phosphorylated NCBD, with Pro20 either in *trans* or in *cis*, were used as the starting points of further molecular dynamics simulations at equilibrium. The Cα RMSD differences for NCBD from the deposited NMR structure of the NCBD-ACTR complex (1KBH) were 0.4, 1.4, 0.6, and 2.1 nm for WT, $NCBD_{pS19}$, $NCBD_{pS22}$, and $NCBD_{pS19,\,pS22}$, respectively. The systems were equilibrated as previously described and simulated at a temperature of 298.15 K for a total of 6.4 μs (8 replicates of 1 μs, with the first 200 ns of each replicate considered as equilibration time and removed). The NCBD-ACTR complex was simulated only in the *trans* Pro20 isomer to understand the effect of serine phosphorylation

on the most binding-competent conformation as described from the experiments. All analyses were performed using tools available in GROMACS, custom scripts, or MDAnalysis.[92] RMSD-based clustering analysis of the collected trajectory was performed using the *g_cluster* tool available in GROMACS, employing a cutoff of 0.4 nm and the GROMOS algorithm.[93]

SUPPLEMENTARY MATERIAL

See the supplementary material for additional figures of binding isotherms, characterization of phosphorylated and unphosphorylated samples, surface experiments with immobilized NCoAs, more detailed analysis of the simulations, tables with the sequences of all protein variants used, and values of kinetic and equilibrium analyses of the fluorescence time traces.

ACKNOWLEDGMENTS

We thank Stefanie Jörg and Stephan Baumgartner for assistance with protein expression and purification and with single-molecule experiments of NCBD-SRC1. We thank Hagen Hofmann for helpful discussions and for providing expression plasmids for ACTR and NCBD; Jendrik Schöppe and Andreas Plückthun for the pAT222-pD expression plasmid; and Serge Chesnov at the Functional Genomics Center Zürich for mass spectrometry analysis. This work was supported by the Swiss National Science Foundation, and the Marsden Fund Council from the New Zealand Government funding, managed by the Royal Society Te Apārangi. We utilized the computational resources of Piz Daint at the CSCS Swiss National Supercomputing Centre and the Nectar cloud infrastructure provided by the Center for eResearch at the University of Auckland.

AUTHOR DECLARATIONS

Conflict of Interest

The authors have no conflicts to disclose.

Author Contributions

Karin J. Buholzer: Conceptualization (equal); Data curation (lead); Formal analysis (lead); Investigation (lead); Methodology (equal); Project administration (supporting); Software (supporting); Visualization (lead); Writing – original draft (lead); Writing – review & editing (equal). **Jordan McIvor**: Data curation (lead); Formal analysis (lead); Investigation (lead); Software (equal); Visualization (lead); Writing – review & editing (equal). **Franziska Zosel**: Conceptualization (lead); Data curation (supporting); Formal analysis (supporting); Investigation (equal); Methodology (equal); Software (supporting); Supervision (equal); Writing – review & editing (equal). **Christian Teppich**: Data curation (supporting); Formal analysis (equal); Investigation (equal). **Daniel Nettels**: Conceptualization (supporting); Data curation (equal); Formal analysis (equal); Investigation (supporting); Methodology (equal); Software (lead); Supervision (equal); Visualization (supporting); Writing – review & editing (equal). **Davide Mercadante**: Conceptualization (lead); Data curation (equal); Formal analysis (equal); Funding acquisition (lead); Investigation (equal); Methodology (equal); Project administration (equal); Software (lead); Supervision (lead); Visualization (equal); Writing – review & editing (equal). **Benjamin Schuler**: Conceptualization (lead); Funding acquisition (lead); Methodology (supporting); Project administration (lead); Supervision (lead); Writing – original draft (supporting); Writing – review & editing (lead).

DATA AVAILABILITY

The data that support the findings of this study are available from the corresponding authors upon reasonable request.

REFERENCES

[1] M. Fuxreiter, Á. Tóth-Petróczy, D. A. Kraut, A. T. Matouschek, R. Y. H. Lim, B. Xue, L. Kurgan, and V. N. Uversky, Chem. Rev. **114**, 6806 (2014).
[2] P. E. Wright and H. J. Dyson, Nat. Rev. Mol. Cell Biol. **16**, 18 (2015).
[3] C. J. Oldfield and A. K. Dunker, Annu. Rev. Biochem. **83**, 553 (2014).
[4] R. van der Lee, M. Buljan, B. Lang, R. J. Weatheritt, G. W. Daughdrill, A. K. Dunker, M. Fuxreiter, J. Gough, J. Gsponer, D. T. Jones, P. M. Kim, R. W. Kriwacki, C. J. Oldfield, R. V. Pappu, P. Tompa, V. N. Uversky, P. E. Wright, and M. M. Babu, Chem. Rev. **114**, 6589 (2014).
[5] A. L. Darling and V. N. Uversky, Front. Genet. **9**, 158 (2018).
[6] H. J. Dyson and P. E. Wright, J. Biol. Chem. **291**, 6714 (2016).
[7] A. Bah and J. D. Forman-Kay, J. Biol. Chem. **291**, 6696 (2016).
[8] F. Wiggers, S. Wohl, A. Dubovetskyi, G. Rosenblum, W. Zheng, and H. Hofmann, Proc. Natl. Acad. Sci. U. S. A. **118**, e2106690118 (2021).
[9] B. Schuler, A. Borgia, M. B. Borgia, P. O. Heidarsson, E. D. Holmstrom, D. Nettels, and A. Sottini, Curr. Opin. Struct. Biol. **60**, 66 (2020).
[10] P. Tompa and M. Fuxreiter, Trends Biochem. Sci. **33**, 2 (2008).
[11] R. B. Berlow, H. J. Dyson, and P. E. Wright, J. Mol. Biol. **430**, 2309 (2018).
[12] P. E. Wright and H. J. Dyson, Curr. Opin. Struct. Biol. **19**, 31 (2009).
[13] S. Gianni, J. Dogan, and P. Jemth, Curr. Opin. Struct. Biol. **36**, 18 (2016).
[14] V. J. Hilser, J. O. Wrabl, and H. N. Motlagh, Annu. Rev. Biophys. **41**, 585 (2012).
[15] A. C. M. Ferreon, J. C. Ferreon, P. E. Wright, and A. A. Deniz, Nature **498**, 390 (2013).
[16] V. Csizmok and J. D. Forman-Kay, Curr. Opin. Struct. Biol. **48**, 58 (2018).
[17] R. Nussinov, C.-J. Tsai, F. Xin, and P. Radivojac, Trends Biochem. Sci. **37**, 447 (2012).
[18] J. Liu, N. B. Perumal, C. J. Oldfield, E. W. Su, V. N. Uversky, and A. K. Dunker, Biochemistry **45**, 6873 (2006).
[19] K. Bugge, L. Staby, E. Salladini, R. G. Falbe-Hansen, B. B. Kragelund, and K. Skriver, J. Biol. Chem. **296**, 100226 (2020).
[20] S. J. Demarest, M. Martinez-Yamout, J. Chung, H. Chen, W. Xu, H. J. Dyson, R. M. Evans, and P. E. Wright, Nature **415**, 549 (2002).
[21] M. Kjaergaard, K. Teilum, and F. M. Poulsen, Proc. Natl. Acad. Sci. U. S. A. **107**, 12535 (2010).
[22] C. H. Lin, B. J. Hare, G. Wagner, S. C. Harrison, T. Maniatis, and E. Fraenkel, Mol. Cell **8**, 581 (2001).
[23] X.-H. Feng, Y. Zhang, R.-Y. Wu, and R. Derynck, Genes Dev. **12**, 2153 (1998).
[24] K. E. S. Scoggin, A. Ulloa, and J. K. Nyborg, Mol. Cell. Biol. **21**, 5520 (2001).
[25] S. Gingras, J. Simard, B. Groner, and E. Pfitzner, Nucleic Acids Res. **27**, 2722 (1999).
[26] L. Waters, B. Yue, V. Veverka, P. Renshaw, J. Bramham, S. Matsuda, T. Frenkiel, G. Kelly, F. Muskett, M. Carr, and D. M. Heery, J. Biol. Chem. **281**, 14787 (2006).
[27] J. C. Ferreon, C. W. Lee, M. Arai, M. A. Martinez-Yamout, H. J. Dyson, and P. E. Wright, Proc. Natl. Acad. Sci. U. S. A. **106**, 6591 (2009).
[28] C. W. Lee, M. A. Martinez-Yamout, H. J. Dyson, and P. E. Wright, Biochemistry **49**, 9964 (2010).
[29] B. Y. Qin, C. Liu, H. Srinath, S. S. Lam, J. J. Correia, R. Derynck, and K. Lin, Structure **13**, 1269 (2005).
[30] S. J. Demarest, S. Deechongkit, H. J. Dyson, R. M. Evans, and P. E. Wright, Protein Sci. **13**, 203 (2004).

[31] J. Dogan, T. Schmidt, X. Mu, Å. Engström, and P. Jemth, J. Biol. Chem. **287**, 34316 (2012).
[32] M. Kjaergaard, L. Andersen, L. D. Nielsen, and K. teilum, Biochemistry **52**, 1686 (2013).
[33] J. Dogan, X. Mu, Å. Engström, and P. Jemth, Sci. Rep. **3**, 2076 (2013).
[34] V. Ješmantavičius, M. R. Jensen, V. Ozenne, M. Blackledge, F. M. Poulsen, and M. Kjaergaard, J. Am. Chem. Soc. **135**, 10155 (2013).
[35] P. Jemth, X. Mu, Å. Engström, and J. Dogan, J. Biol. Chem. **289**, 5528 (2014).
[36] V. Ješmantavičius, J. Dogan, P. Jemth, K. teilum, and M. Kjaergaard, Angew. Chem., Int. Ed. **53**, 1548 (2014).
[37] F. Zosel, D. Mercadante, D. Nettels, and B. Schuler, Nat. Commun. **9**, 3332 (2018).
[38] F. Sturzenegger, F. Zosel, E. D. Holmstrom, K. J. Buholzer, D. E. Makarov, D. Nettels, and B. Schuler, Nat. Commun. **9**, 4708 (2018).
[39] F. Zosel, A. Soranno, K. J. Buholzer, D. Nettels, and B. Schuler, Proc. Natl. Acad. Sci. U. S. A. **117**, 13480 (2020).
[40] J. Dogan, J. Jonasson, E. Andersson, and P. Jemth, Biochemistry **54**, 4741 (2015).
[41] N. Dephoure, C. Zhou, J. Villén, S. A. Beausoleil, C. E. Bakalarski, S. J. Elledge, and S. P. Gygi, Proc. Natl. Acad. Sci. U. S. A. **105**, 10762 (2008).
[42] V. Mayya, D. H. Lundgren, S. I. Hwang, K. Rezaul, L. Wu, J. K. Eng, V. Rodionov, and D. K. Han, Sci. Signaling **2**, ra46 (2009).
[43] A. N. Kettenbach, D. K. Schweppe, B. K. Faherty, D. Pechenick, A. A. Pletnev, and S. A. Gerber, Sci. Signaling **4**, rs5 (2011).
[44] K. Sharma, R. C. J. D'Souza, S. Tyanova, C. Schaab, J. R. Wiśniewski, J. Cox, and M. Mann, Cell Rep. **8**, 1583 (2014).
[45] V. Bauer, B. Schmidtgall, G. Gogl, J. Dolenc, J. Osz, Y. Nomine, C. Kostmann, A. Cousido-Siah, A. Mitschler, N. Rochel, G. Trave, B. Kieffer, and V. Torbeev, Chem. Sci. **12**, 1080 (2021).
[46] P. Haberz, M. Arai, M. A. Martinez-Yamout, H. J. Dyson, and P. E. Wright, Protein Sci. **25**, 2256 (2016).
[47] G. Manning, D. B. Whyte, R. Martinez, T. Hunter, and S. Sudarsanam, Science **298**, 1912 (2002).
[48] P. V. Hornbeck, B. Zhang, B. Murray, J. M. Kornhauser, V. Latham, and E. Skrzypek, Nucleic Acids Res. **43**, D512 (2015).
[49] J. A. Ubersax and J. E. Ferrell, Jr., Nat. Rev. Mol. Cell Biol. **8**, 530 (2007).
[50] R. Roy, S. Hohng, and T. Ha, Nat. Methods **5**, 507 (2008).
[51] J. J. Benítez, A. M. Keller, and P. Chen, Methods Enzymol. **472**, 41 (2010).
[52] A. M. van Oijen, Curr. Opin. Biotechnol. **22**, 75 (2011).
[53] J.-Y. Kim, F. Meng, J. Yoo, and H. S. Chung, Nat. Commun. **9**, 4707 (2018).
[54] M. Schutkowski, A. Bernhardt, X. Z. Zhou, M. Shen, U. Reimer, J.-U. Rahfeld, K. P. Lu, and G. Fischer, Biochemistry **37**, 5566 (1998).
[55] E. B. Gibbs, F. Y. Lu, B. Portz, M. J. Fisher, B. P. Medellin, T. N. Laremore, Y. J. Zhang, D. S. Gilmour, and S. A. Showalter, Nat. Commun. **8**, 15233 (2017).
[56] L. Alessandro and L. G. Francesco, Rep. Prog. Phys. **71**, 126601 (2008).
[57] E. W. Martin, A. S. Holehouse, C. R. Grace, A. Hughes, R. V. Pappu, and T. Mittag, J. Am. Chem. Soc. **138**, 15323 (2016).
[58] M. D. Crabtree, W. Borcherds, A. Poosapati, S. L. Shammas, G. W. Daughdrill, and J. Clarke, Biochemistry **56**, 2379 (2017).
[59] C. W. Lee, J. C. Ferreon, A. C. M. Ferreon, M. Arai, and P. E. Wright, Proc. Natl. Acad. Sci. U. S. A. **107**, 19290 (2010).
[60] J. Guo and H.-X. Zhou, Chem. Rev. **116**, 6503 (2016).
[61] S. Dasgupta, D. M. Lonard, and B. W. O'Malley, Annu. Rev. Med. **65**, 279 (2014).
[62] J. Xu and Q. Li, Mol. Endocrinol. **17**, 1681 (2003).
[63] P. Yi, Z. Wang, Q. Feng, G. D. Pintilie, C. E. Foulds, R. B. Lanz, S. J. Ludtke, M. F. Schmid, W. Chiu, and B. W. O'Malley, Mol. Cell **57**, 1047 (2015).
[64] L. Ma, Z. Gao, J. Wu, B. Zhong, Y. Xie, W. Huang, and Y. Lin, Mol. Cell **81**, 1682 (2021).
[65] D. Guin and M. Gruebele, Chem Rev **119**, 10691 (2019).
[66] S. S. Stadmiller and G. J. Pielak, Curr. Opin. Struct. Biol. **66**, 183 (2020).
[67] R. Vancraenenbroeck, Y. S. Harel, W. Zheng, and H. Hofmann, Proc. Natl. Acad. Sci. U. S. A. **116**, 19506 (2019).
[68] J. Schilling, J. Schoppe, and A. Pluckthun, J. Mol. Biol. **426**, 691 (2014).
[69] A. Borgia, W. Zheng, K. Buholzer, M. B. Borgia, A. Schüler, H. Hofmann, A. Soranno, D. Nettels, K. Gast, A. Grishaev, R. B. Best, and B. Schuler, J. Am. Chem. Soc. **138**, 11714 (2016).
[70] G. L. Ellman, Arch. Biochem. Biophys. **74**, 443 (1958).
[71] D. Nettels, S. Müller-Späth, F. Küster, H. Hofmann, D. Haenni, S. Rüegger, L. Reymond, A. Hoffmann, J. Kubelka, B. Heinz, K. Gast, R. B. Best, and B. Schuler, Proc. Natl. Acad. Sci. U. S. A. **106**, 20740 (2009).
[72] B. Schuler, Methods. Mol. Biol. **350**, 115 (2007).
[73] S. Benke, D. Nettels, H. Hofmann, and B. Schuler, Nanotechnology **28**, 114002 (2017).
[74] J. R. Lakowicz, *Principles of Fluorescence Spectroscopy*, 3rd ed. (Springer, New York, 2006).
[75] T. Ha and P. Tinnefeld, Annu. Rev. Phys. Chem. **63**, 595 (2012).
[76] J. Vogelsang, R. Kasper, C. Steinhauer, B. Person, M. Heilemann, M. Sauer, and P. Tinnefeld, Angew. Chem., Int. Ed. **47**, 5465 (2008).
[77] J. Enderlein, I. Gregor, D. Patra, T. Dertinger, and U. B. Kaupp, ChemPhysChem **6**, 2324 (2005).
[78] M. Blanco and N. G. Walter, Methods Enzymol. **472**, 153 (2010).
[79] S. A. McKinney, C. Joo, and T. Ha, Biophys. J. **91**, 1941 (2006).
[80] D. Van Der Spoel, E. Lindahl, B. Hess, G. Groenhof, A. E. Mark, and H. J. C. Berendsen, J. Comput. Chem. **26**, 1701 (2005).
[81] H. J. C. Berendsen, D. van der Spoel, and R. van Drunen, Comput. Phys. Commun. **91**, 43 (1995).
[82] P. Robustelli, S. Piana, and D. E. Shaw, Proc. Natl. Acad. Sci. U. S. A. **115**, E4758 (2018).
[83] N. Homeyer, A. H. C. Horn, H. Lanig, and H. Sticht, J. Mol. Model. **12**, 281 (2006).
[84] S. Piana, A. G. Donchev, P. Robustelli, and D. E. Shaw, J. Phys. Chem. B **119**, 5113 (2015).
[85] G. Bussi, D. Donadio, and M. Parrinello, J. Chem. Phys. **126**, 014101 (2007).
[86] M. Parrinello and A. Rahman, J. Appl. Phys. **52**, 7182 (1981).
[87] B. Hess, H. Bekker, H. J. C. Berendsen, and J. G. E. M. Fraaije, J. Comput. Chem. **18**, 1463 (1997).
[88] T. Darden, D. York, and L. Pedersen, J. Chem. Phys. **98**, 10089 (1993).
[89] L. Verlet, Phys. Rev. **159**, 98 (1967).
[90] A. Barducci, G. Bussi, and M. Parrinello, Phys. Rev. Lett. **100**, 020603 (2008).
[91] M. Bonomi, D. Branduardi, G. Bussi, C. Camilloni, D. Provasi, P. Raiteri, D. Donadio, F. Marinelli, F. Pietrucci, R. A. Broglia, and M. Parrinello, Comput. Phys. Commun. **180**, 1961 (2009).
[92] N. Michaud-Agrawal, E. J. Denning, T. B. Woolf, and O. Beckstein, J. Comput. Chem. **32**, 2319 (2011).
[93] X. Daura, K. Gademann, B. Jaun, D. Seebach, W. F. van Gunsteren, and A. E. Mark, Angew. Chem. Int. Ed. **38**, 236 (1999).

Supplementary Information

Multilayered allosteric modulation of coupled folding and binding by phosphorylation, peptidyl-prolyl *cis*/*trans* isomerization, and diversity of interaction partners

Karin J. Buholzer[1,2], Jordan McIvor[3], Franziska Zosel[1,4], Christian Teppich[1], Daniel Nettels[1], Davide Mercadante[1,3], and Benjamin Schuler[1,5]

[1]Department of Biochemistry, University of Zurich, Zurich, Switzerland

[2]Present address: Center for Microscopy and Image Analysis, University of Zurich, Zurich, Switzerland

[3]School of Chemical Sciences, The University of Auckland, Auckland, New Zealand

[4]Present address: Department of Biophysics and Injectable Formulation 2, Novo Nordisk A/S, Måløv, Denmark

[5]Department of Physics, University of Zurich, Zurich, Switzerland

To whom correspondence should be addressed:

D. Mercadante: davide.mercadante@auckland.ac.nz, B. Schuler: schuler@bioc.uzh.ch

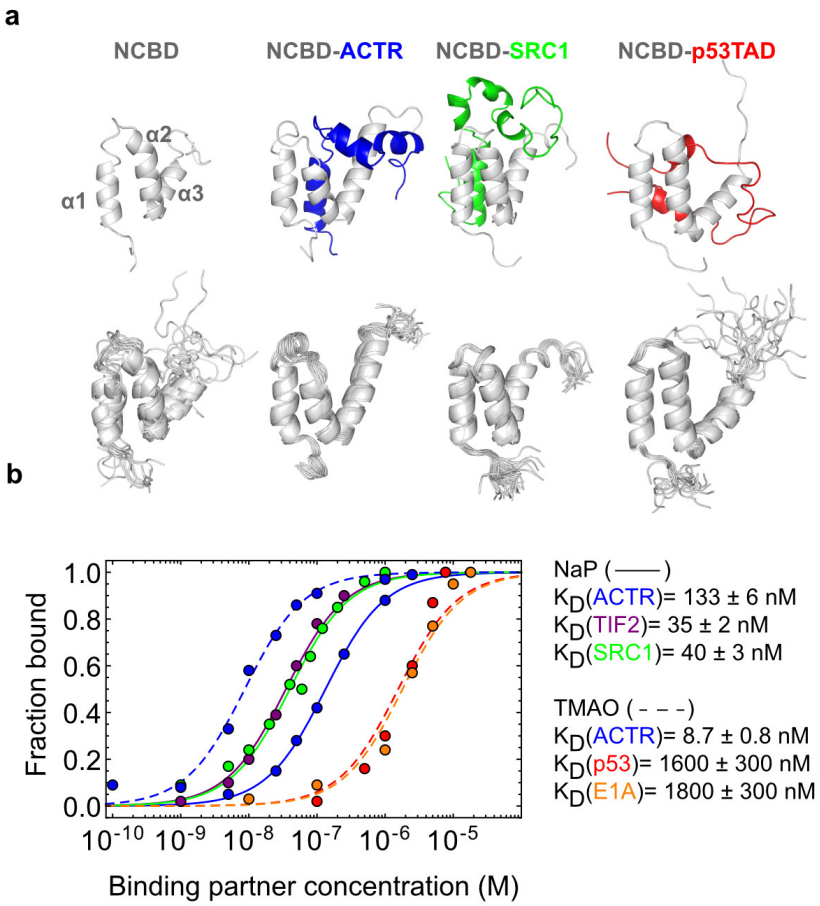

Fig. S1. **Binding of NCBD with its disordered binding partners.** a) NMR structures of free NCBD (gray, with helices α1-α3 indicated), NCBD bound to ACTR (blue), SRC1 (green), and p53TAD (red). To highlight the different degrees of disorder in the flexible tails of NCBD, NMR conformers of the respective structures of NCBD are overlaid below (PDB 2KKJ[1], 1KBH[2], 2C52[3], 2L14[4]). b) Fractions of bound NCBD as a function of binding partner concentrations (see legend), fitted with binding isotherms. Errors represent the standard errors of the fits. Even in the presence of the stabilizing osmolyte trimethylamine oxide (TMAO)[5, 6], p53TAD and E1A show equilibrium dissociation constants (K_D) with NCBD in the micromolar range, too high for intermolecular FRET experiments. Therefore, we focus our kinetic studies on the NCoAs ACTR, TIF2, and SRC1 binding to NCBD.

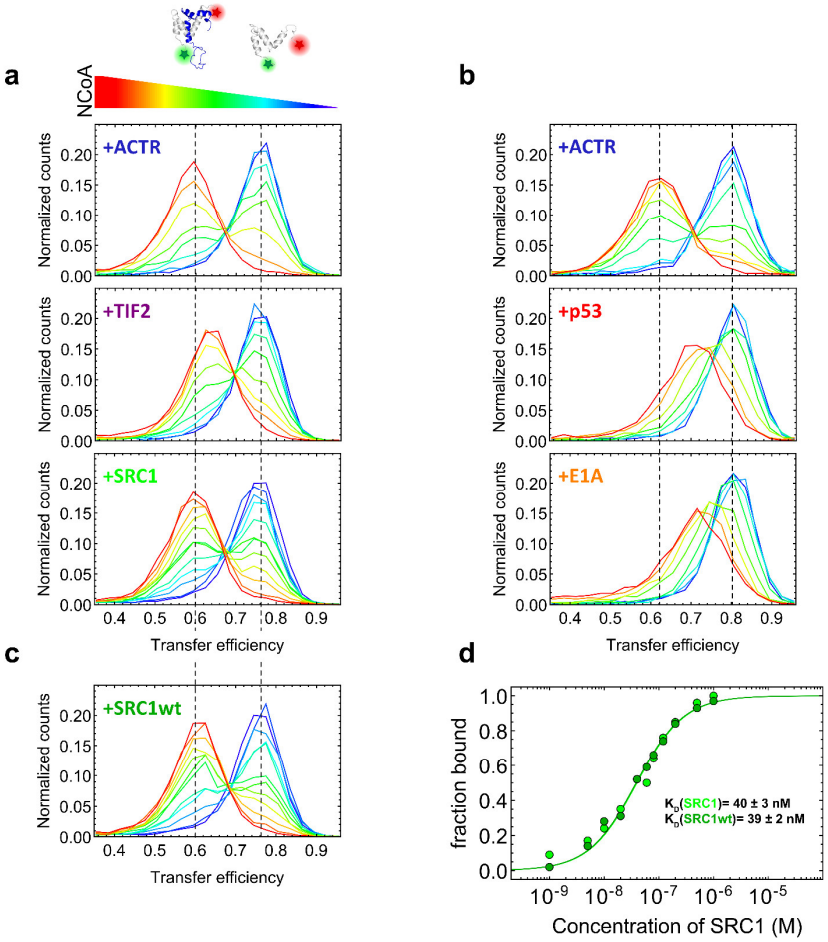

Fig. S2 **Titrations of NCBD with different binding partners.** Double-labeled NCBD (Alexa Fluor 488, Biotium CF660R) binding to increasing concentrations of its partners. The transfer efficiency histograms are normalized to unit area under the peaks. The dashed lines indicate the transfer efficiencies of unbound NCBD (high *E*) and ACTR-bound NCBD (low *E*) for comparison. a) Interaction of NCBD with the three NCoAs ACTR, TIF2, and SRC1 in phosphate buffer. b) NCBD binding to ACTR, p53, and E1A in the presence of 1M TMAO. c) NCBD binding to SRC1wt, containing the two naturally occurring Cys in the N-terminal tail (Table S). d) The fraction of bound NCBD as a function of binding partner concentration, fitted with binding isotherms to determine K_D in the presence (SRC1wt) and absence (SRC1) of the two N-terminal Cys residues. Errors represent the standard errors of the fits.

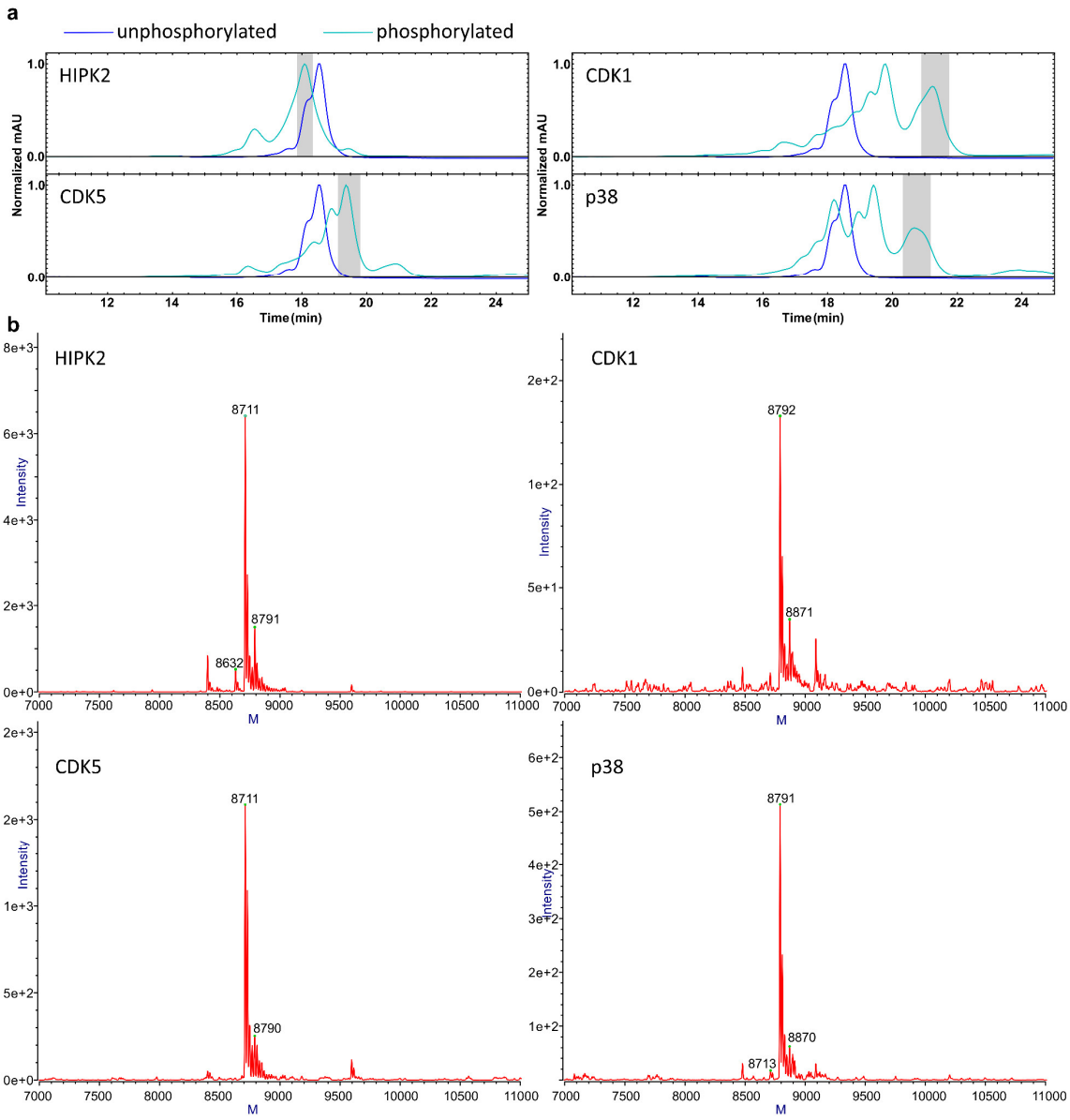

Fig. S3 **Enzymatic phosphorylation of double-labeled NCBD.** a) RP-HPLC chromatograms indicating the shift in retention times upon phosphorylation of NCBD (light blue) compared to the unphosphorylated NCBD (dark blue). The kinases used are indicated in the panels. Note that CDK1- and p38-phosphorylated NCBD were run on different days, therefore the absolute retention times are slightly shifted. The peaks indicated in gray were collected for further analysis. b) Electrospray ionization mass spectrometry of the peaks indicated in a). Double-labeled NCBD has a molecular weight of 8632 Da, with each phosphorylation adding 80 Da: modification with one phosphate group corresponds to 8712 Da, with two phosphate groups to 8792 Da, and with three phosphate groups to 8872 Da.

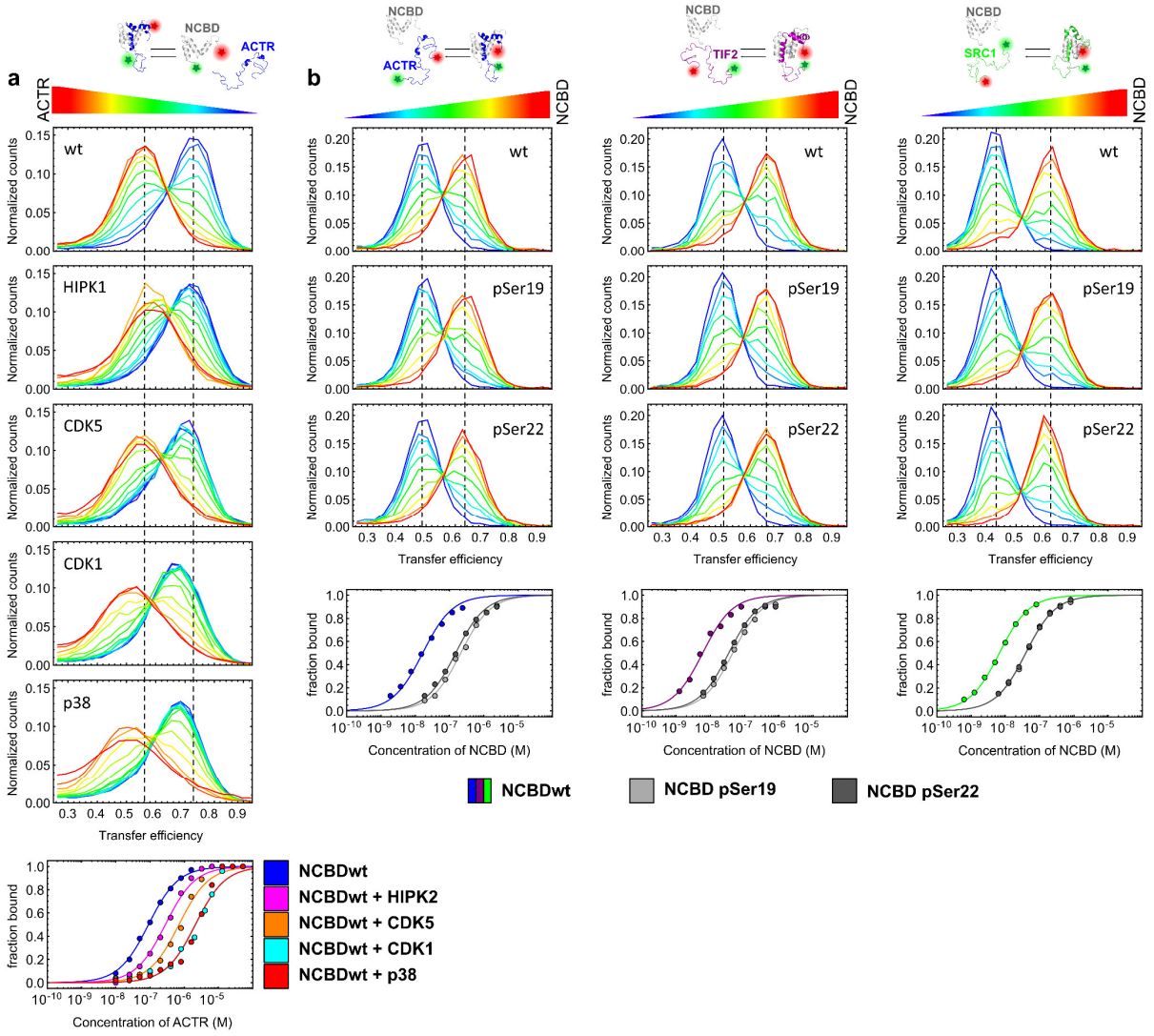

Fig. S4 **The effect of phosphorylation on different binding interactions.** a) Double-labeled NCBD (Alexa 488/CF660R) phosphorylated with different kinases (as indicated) binding to unlabeled ACTR. b) Double-labeled ACTR, TIF2, and SRC1 (Alexa 488/594) binding to chemically synthesized NCBD in the absence (wt) or presence of phosphorylation (pSer19 and pSer22). All transfer efficiency histograms are normalized to unit area under the peaks. The fraction of labeled and bound NCBD (a) or NCoAs (b) as a function of binding partner concentration fitted with a binding isotherm to determine K_D. The structures of free NCBD (2KKJ[1]) and in complex with ACTR (PDB: 1KBH[2]), TIF2, and SRC1 (PDB: 2C52[3]) are shown for illustration. Please note that the structure of the TIF2-NCBD complex is based on a model generated by swissmodel[7] and does not represent an experimentally determined structure.

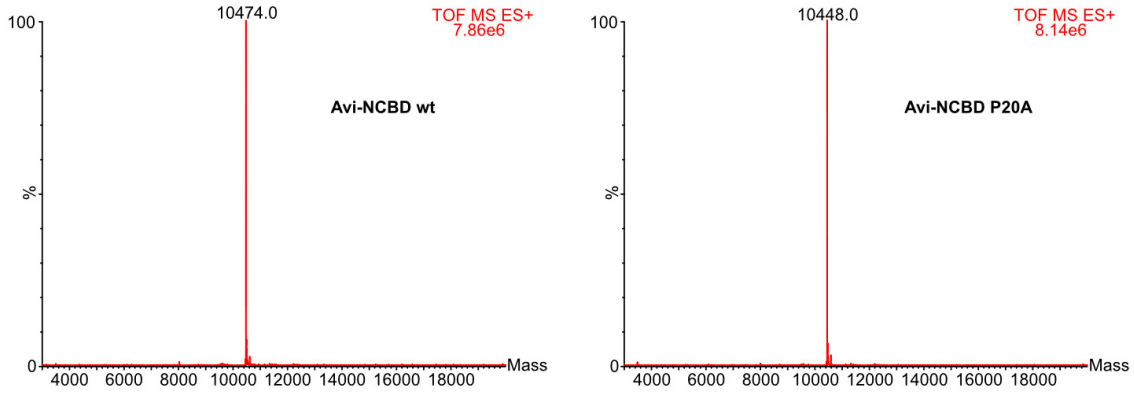

Fig. S5 **ESI-MS of Avi-NCBD wt and Avi-NCBD P20A with expected masses of 10'474 Da and 10'448 Da, respectively.**

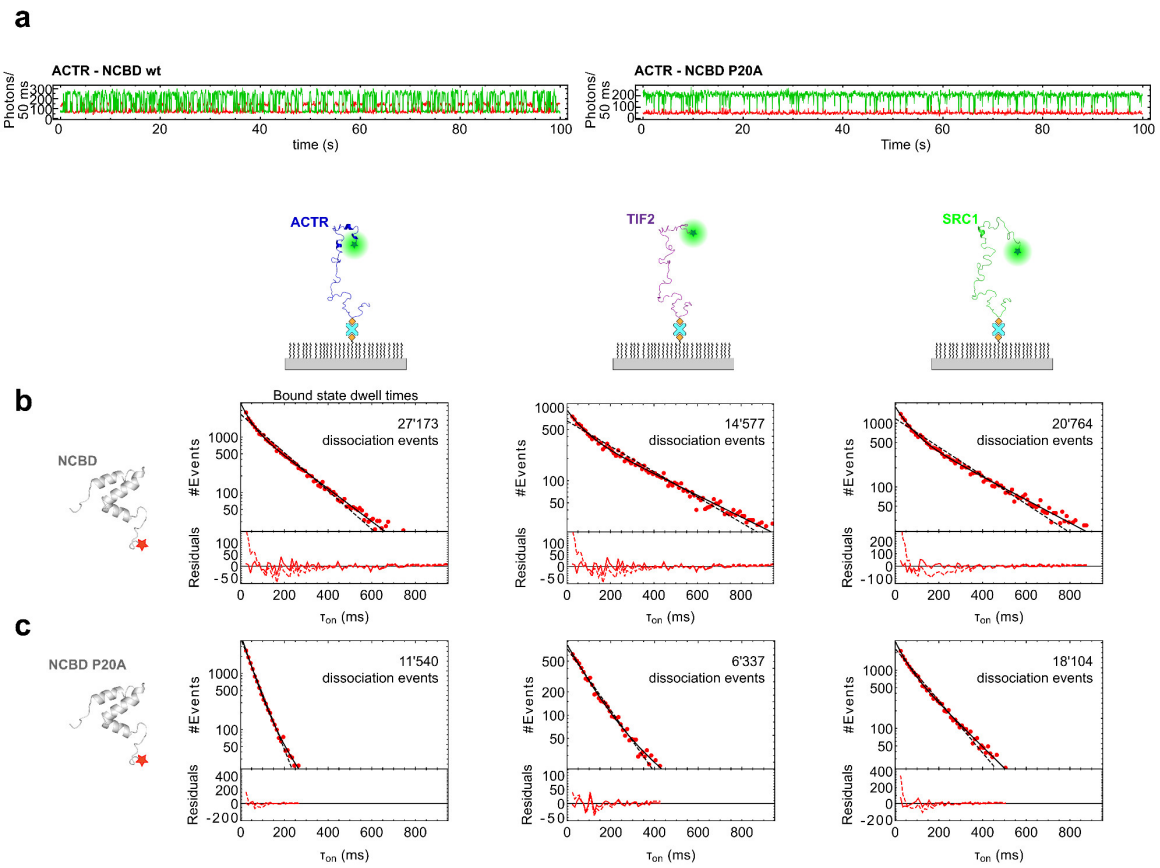

Fig. S6 **Immobilized NCoAs binding to NCBD.** a) Representative time traces of immobilized ACTR binding to NCBD wt and NCBD P20A. b) and c) Dwell-time histograms of immobilized ACTR, TIF2, and SRC1 binding to NCBD wt (b) or NCBD P20A (c) with single- (dashed line) and double-exponential fits to the dwell-time distributions. The residuals are plotted accordingly.

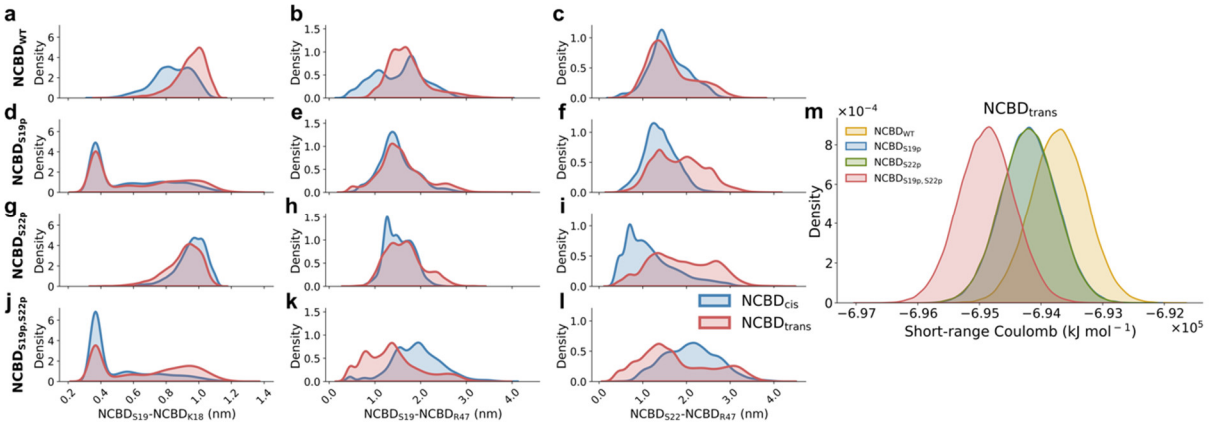

Fig. S7 **Electrostatic interactions within the unbound NCBD ensemble.** Probability density functions of the distances between Ser19 and Lys18, Ser19 and Arg47, or Ser22 and Arg47 for the *cis* (blue) and *trans* (red) ensembles when NCBD is either unphosphorylated (a-c), phosphorylated on Ser19 (d-f), phosphorylated on Ser22 (g-i), and doubly phosphorylated (j-l). m) Probability density function of the short-range Coulomb energy obtained from the simulation of unphosphorylated NCBD (gold) and NCBD phosphorylated on Ser19 (blue), Ser22 (green), or both (red).

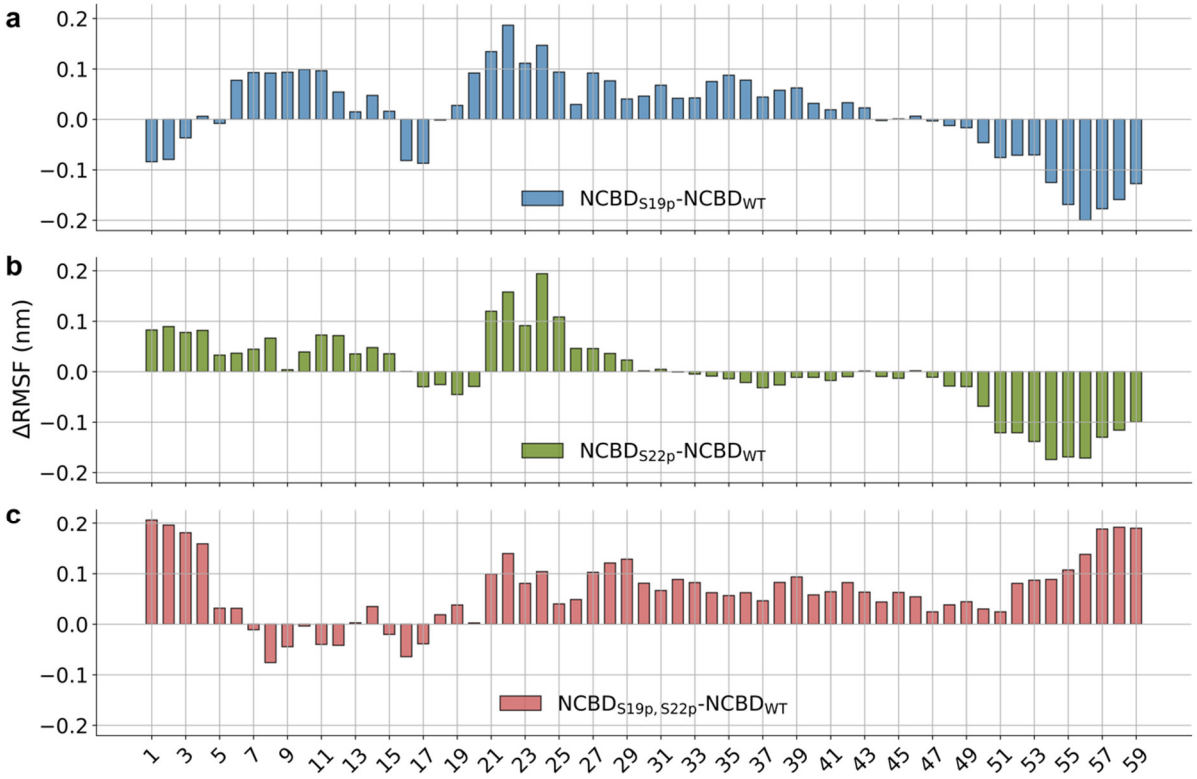

Fig. S8 **Changes in residue-specific root mean square fluctuations (RMSF) of NCBD upon phosphorylation from MD simulations of the NCBD-ACTR complex.** The difference in RMSF between unphosphorylated and phosphorylated NCBD (ΔRMSF) when the protein is either phosphorylated on Ser19 (a), Ser22 (b), or doubly phosphorylated (c).

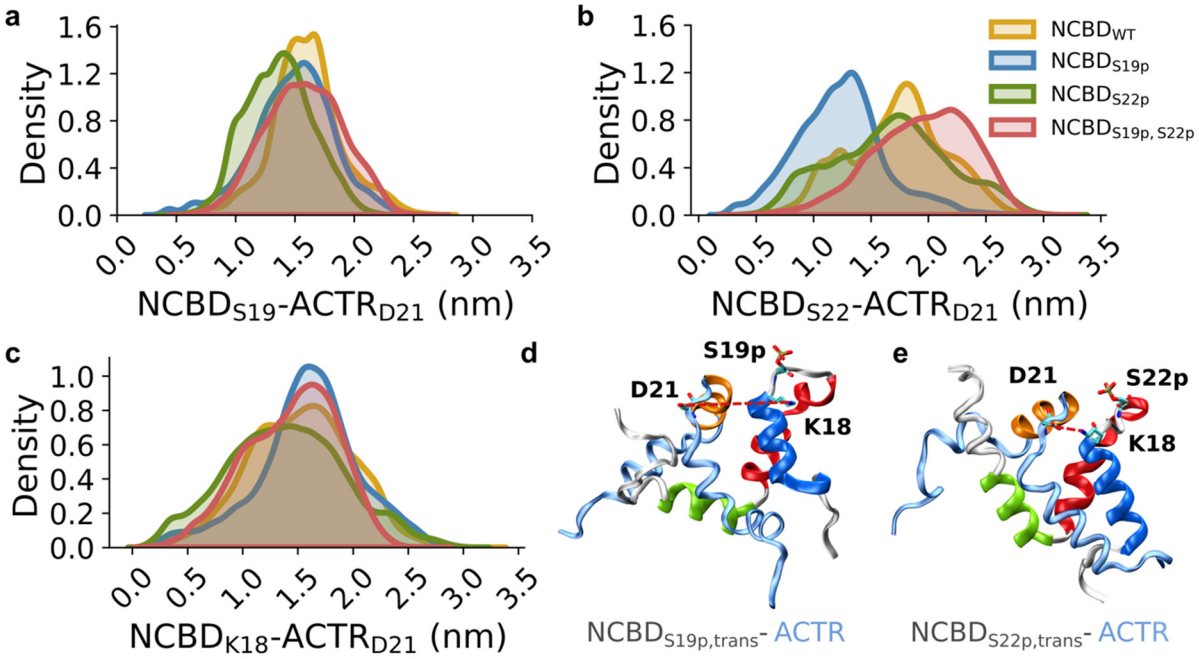

Fig. S9 **Interplay of charged amino acids within the NCBD-ACTR complex.** Probability density functions of the distance between NCBD Ser19 (a), Ser22 (b), or K18 (c) and ACTR Asp21 when NCBD is either unphosphorylated (gold), phosphorylated on Ser19 (blue), phosphorylated on Ser22 (green), or doubly phosphorylated (red). d-e) Representative conformations illustrating the positions of these residues to highlight their proximity in the NCBD-ACTR complex.

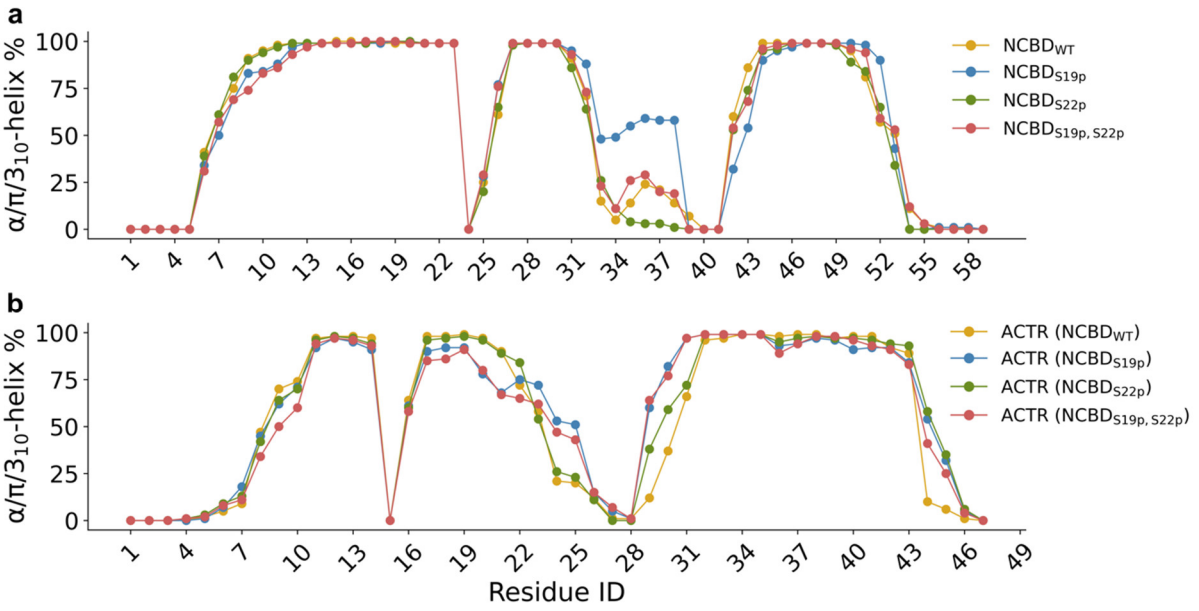

Fig. S10 **Helical content for NCBD and ACTR from MD simulations in the NCBD-ACTR complex.** The sum of α-, π-, and 3_{10} – helical content (%), as obtained from the DSSP algorithm[8], is shown for NCBD (a) and ACTR (b) when NCBD is unphosphorylated (gold), phosphorylated on Ser19 (blue), phosphorylated on Ser22 (green), or doubly phosphorylated (red).

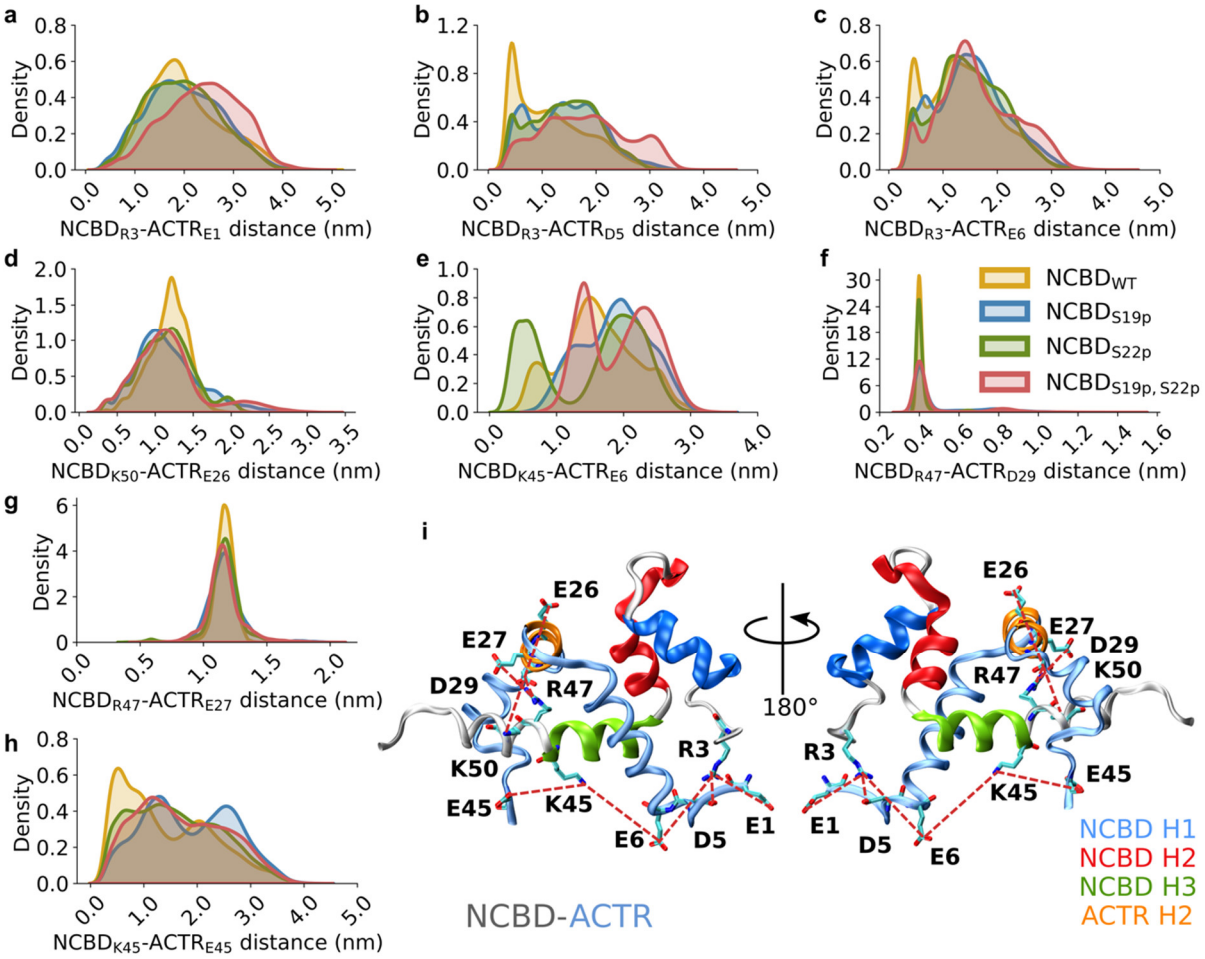

Fig. S11 **Effects of distally positioned charged amino acids within the NCBD-ACTR complex.** (a-h) probability density functions of the distance between positively charged residues in NCBD and negatively charged residues in ACTR when NCBD is either unphosphorylated (gold), phosphorylated on Ser19 (blue), phosphorylated on Ser22 (green), or doubly phosphorylated (red). i) A representative structure of the NCBD-ACTR complex illustrating the distal salt-bridge network within the NCBD-ACTR complex.

Table S 1 **Amino acid sequences and fluorophores of the protein variants used in this study** (after proteolytic removal of the His_6-tag). The Cys residues introduced for labeling with fluorophores are marked in red, the biotinylated Lys in the Avi-tag in blue, the phosphorylated Ser residues (pS) in green, and residues not corresponding to the naturally occurring sequences are underlined (apart from the Avi-tag and the residues corresponding to the 3C- and thrombin cleavage site). The sequences correspond to human ACTR 1018-1088 (UniProt Q9Y6Q9, isoform 3), human TIF2 1049-1116 (UniProt Q15596), human SRC1 902-971 (Q15788, isoform 1), human p53 13-61 (UniProt P04637, isoform 1), human adenovirus A serotype 12 35-81 (UniProt P03259, isoform 1), and human CBP 2060-2116 (UniProt Q92793, isoform 1). Five different fluorophores were used in different combinations: Alexa Fluor 488 and 594 (ThermoFisher), CF660R and CF680R (Biotium), and Cy3B (Cytiva).

Protein	Fluoro-phores	Sequence
Free diffusion experiments Fig.1 and Fig. S1/2		
NCBD DL	A488& CF660R	GPCPNRSISPSALQDLLRTLKSPSSPQQQQQVLNILKSNPQLMAAFIKQRTAK YVANQPGMQC
ACTR	-	GPSGTQNRPLLRNSLDDLVGPPSNLEGQSDERALLDQLHTLLSNTDATGLEEI DRALGIPELVNQGQALEPKQDCGGPR
TIF2	-	GPSASQNRQPFGSSPDDLLSPHPAAESPSDEGALLDQLYLALRNFDGLEEIDR ALGIPELVSQSQAVDPEQCGGPR
SRC1	-	GPSSKSEDQSISSQLDELLSPPTTVEGRNDEKALLEQLVSFLSGKDETELAELD RALGIDKLVQGGGLDVLSECGGPR
p53TAD	-	GPSPLSQETFSDLWKLLPENNVLSPLPSQAMDDLMLSPDDIEQWFTEDPGPD CGGPR
E1A	-	GPSDLYVPSLYELYDLDVESAGEDNNEQAVNEFFPESLILAASEGLFLPECGG PR
SRC1 wt	-	GPSSKSEDQCISSQLDELLCPPTTVEGRNDEKALLEQLVSFLSGKDETELAEL DRALGIDKLVQGGGLDVLSECGGPR
Free diffusion experiments Fig. 2 and Fig. S3/4		
NCBD DL	A488& CF660R	GPCPNRSISPSALQDLLRTLKSPSSPQQQQQVLNILKSNPQLMAAFIKQRTAK YVANQPGMQC
ACTR noCys	-	GPGTQNRPLLRNSLDDLVGPPSNLEGQSDERALLDQLHTLLSNTDATGLEEID RALGIPELVNQGQALEPKQD
ACTR DL	A488& A594	GPCGTQNRPLLRNSLDDLVGPPSNLEGQSDERALLDQLHTLLSNTDATGLEEI DRALGIPELVNQGQALEPKQDCGGPR
TIF2 DL	A488& A594	GPCASQNRQPFGSSPDDLLSPHPAAESPSDEGALLDQLYLALRNFDGLEEIDR ALGIPELVSQSQAVDPEQCGGPR
SRC1 DL	A488& A594	GPCSKSEDQSISSQLDELLSPPTTVEGRNDEKALLEQLVSFLSGKDETELAEL DRALGIDKLVQGGGLDVLSECGGPR
NCBDwt	-	GSMGSGSSPNRSISPSALQDLLRTLKSPSSPQQQQQVLNILKSNPQLMAAFIK QRTAKYVANQPGMQCGGPR
NCBD pSer19	-	GSMGSGSSPNRSISPSALQDLLRTLKpSPSSPQQQQQVLNILKSNPQLMAAFIK QRTAKYVANQPGMQCGGPR
NCBD pSer22	-	GSMGSGSSPNRSISPSALQDLLRTLKSPSpSPQQQQQVLNILKSNPQLMAAFIK QRTAKYVANQPGMQCGGPR
Surface experiments Fig. 3 and Fig. S5/6		
Avi-ACTR	Cy3B	AGLNDIFEAQKIEWHEGSMGSGSLEVLFQ GPSGTQNRPLLRNSLDDLVGPPSNLEGQSDERALLDQLHTLLSNTDATGLEEI DRALGIPELVNQGQALEPKQDCGGPR
Avi-TIF2	Cy3B	AGLNDIFEAQKIEWHEGSMGSGSLEVLFQ GPSASQNRQPFGSSPDDLLSPHPAAESPSDEGALLDQLYLALRNFDGLEEIDR ALGIPELVSQSQAVDPEQCGGPR

Avi-SRC1	Cy3B	AGLNDIFEAQKIEWHEGSMGSGSLEVLFQ GPSSKSEDQSISSQLDELLSPPTTVEGRNDEKALLEQLVSFLSGKDETELAELD RALGIDKLVQGGGLDVLSECGGPR
NCBD	CF680R	GPCPNRSISPSALQDLLRTLKSPSSPQQQQQVLNILKSNPQLMAAFIKQRTAK YVANQPGMQ
NCBD P20A	CF680R	GPCPNRSISPSALQDLLRTLKSASSPQQQQQVLNILKSNPQLMAAFIKQRTAK YVANQPGMQC
Avi-NCBD	Cy3B	AGLNDIFEAQKIEWHEGSMGSGS SPNRSISPSALQDLLRTLKSPSSPQQQQQVLNILKSNPQLMAAFIKQRTAKYV ANQPGMQCGGPR
Avi-NCBD P20A	Cy3B	AGLNDIFEAQKIEWHEGSMGSGS SPNRSISPSALQDLLRTLKSASSPQQQQQVLNILKSNPQLMAAFIKQRTAKYV ANQPGMQCGGPR
ACTR	CF660R	GPSGTQNRPLLRNSLDDLVGPPSNLEGQSDERALLDQLHTLLSNTDATGLEEI DRALGIPELVNQGQALEPKQDCGGPR
TIF2	CF660R	GPSASQNRQPFGSSPDDLLSPHPAAESPSDEGALLDQLYLALRNFDGLEEIDR ALGIPELVSQSQAVDPEQCGGPR
SRC1	CF660R	GPSSKSEDQSISSQLDELLSPPTTVEGRNDEKALLEQLVSFLSGKDETELAELD RALGIDKLVQGGGLDVLSECGGPR
Surface experiments Fig. 4		
Avi-ACTR	Cy3B	AGLNDIFEAQKIEWHEGSMGSGSLEVLFQ GPSGTQNRPLLRNSLDDLVGPPSNLEGQSDERALLDQLHTLLSNTDATGLEEI DRALGIPELVNQGQALEPKQDCGGPR
Avi-TIF2	Cy3B	AGLNDIFEAQKIEWHEGSMGSGSLEVLFQ GPSASQNRQPFGSSPDDLLSPHPAAESPSDEGALLDQLYLALRNFDGLEEIDR ALGIPELVSQSQAVDPEQCGGPR
NCBDwt	CF680R	GSMGSGSSPNRSISPSALQDLLRTLKSPSSPQQQQQVLNILKSNPQLMAAFIK QRTAKYVANQPGMQCGGPR
NCBD pSer19	CF680R	GSMGSGSSPNRSISPSALQDLLRTLKpSPSSPQQQQQVLNILKSNPQLMAAFIK QRTAKYVANQPGMQCGGPR
NCBD pSer22	CF680R	GSMGSGSSPNRSISPSALQDLLRTLKSPSpSPQQQQQVLNILKSNPQLMAAFIK QRTAKYVANQPGMQCGGPR
Avi-NCBDwt	Cy3B	KIEWHEGSMGSGSSPNRSISPSALQDLLRTLKSPSSPQQQQQVLNILKSNPQL MAAFIKQRTAKYVANQPGMQCGGPR
Avi-NCBD pSer19	Cy3B	KIEWHEGSMGSGSSPNRSISPSALQDLLRTLKpSPSSPQQQQQVLNILKSNPQL MAAFIKQRTAKYVANQPGMQCGGPR
Avi-NCBD pSer22	Cy3B	KIEWHEGSMGSGSSPNRSISPSALQDLLRTLKSPSpSPQQQQQVLNILKSNPQL MAAFIKQRTAKYVANQPGMQCGGPR
ACTR	CF660R	GPSGTQNRPLLRNSLDDLVGPPSNLEGQSDERALLDQLHTLLSNTDATGLEEI DRALGIPELVNQGQALEPKQDCGGPR
TIF2	CF660R	GPSASQNRQPFGSSPDDLLSPHPAAESPSDEGALLDQLYLALRNFDGLEEIDR ALGIPELVSQSQAVDPEQCGGPR

Table S2 **Affinities of NCBD with and without phosphorylation to NCoAs.** Either the binding of labeled and phosphorylated NCBD to ACTR, or binding of labeled NCoAs to unlabeled and phosphorylated NCBD were measured. Uncertainties represent the error of the fit.

Labeled NCBD	**unphosphorylated**	**HIPK2**	**CDK5**	**CDK1**	**p38**
NCBD-ACTR	90±3 nM	280±20 nM	700±70 nM	2200±200 nM	2100±300 nM
Labeled NCoAs	**unphosphorylated**	**pSer19**	**pSer22**		
ACTR-NCBD	16 ±1 nM	210±9 nM	150±8 nM		
TIF2-NCBD	6.0±0.4 nM	45±2 nM	34±2 nM		
SRC1-NCBD	6.7±0.2 nM	40±1 nM	39±1 nM		

Table S3 **Kinetic parameters of the NCBD interactions with ACTR, TIF2, and SRC1 (see Fig. 3).** Parameters determined from MLH analyses. "Avi-" indicates the binding partner immobilized on the surface via an avidin tag.

	2-state HMM			4-state HMM					
	k_{on} (μM^{-1} s^{-1})	k_{off} (s^{-1})	K_D (nM)	$k_{on,t}$ (μM^{-1} s^{-1})	$k_{on,c}$ (μM^{-1} s^{-1})	$k_{off,t}$ (s^{-1})	$k_{off,c}$ (s^{-1})	$k_{t\to c}$ (s^{-1})	$k_{c\to t}$ (s^{-1})
AviNCBDwt-ACTR	37	7.6	205	4.8	2.4	6.2	19	0.04	0.04
AviNCBDP20A-ACTR	30	21	699						
AviNCBDwt-TIF2	50	5.3	106	6.1	4.0	4.0	11	0.03	0.02
AviNCBDP20A-TIF2	55	11	207						
AviNCBDwt-SRC1	46	7.5	165	5.2	4.1	5.6	22	0.02	0.03
AviNCBDP20A-SRC1	56	12	209	7.3	3.7	9.7	24	0.04	0.04

Table S4 **Kinetic parameters of the NCBD-ACTR and NCBD-TIF2 interactions (see Fig. 4).** Parameters determined from MLH analyses. The immobilized molecules are marked by "Avi-". The phosphorylation positions are indicated. Note that the relative values of the kinetic parameters in Table S4 and Table S3 are similar, but the absolute values differ, most likely because of the slightly different protein sequences used in the experiments. Similarly, the differences in protein sequences and fluorophores lead to slight differences in K_D values compared to the data shown in **Error! Reference source not found.** and Table S2. f_c is defined as $f_c = (1 - f_t)$.

	2-state HMM			4-state HMM					
	k_{on} (μM^{-1} s^{-1})	k_{off} (s^{-1})	K_D (nM)	$k_{on,t}$ (μM^{-1} s^{-1})	$k_{on,c}$ (μM^{-1} s^{-1})	$k_{off,t}$ (s^{-1})	$k_{off,c}$ (s^{-1})	$k_{t\to c}$ (s^{-1})	$k_{c\to t}$ (s^{-1})
AviNCBD-ACTR	38±4	7.80±0.4	200 ±10	46±3	28±7	6.2±0.1	31±2	0.04±0.01	0.067±0.009
AviNCBDpSer19-ACTR	16±0. 1	23±1	1500 ±60	22±0.4	10±2	19.0±0.4	90±6	0.028±0.004	0.035±0.009
AviNCBDpSer22-ACTR	23±2	27±1	1200±10	29±2	18±2	23±1	47 ±3	0.017±0.006	0.022±0.006
AviNCBD-TIF2	61±3	4.6±1	75±10	95±0.2	35±3	3.8±0.9	10±4	0.099±0.050	0.06±0.01
AviNCBDpSer19-TIF2	43±8	17.0±0.6	410±60	62±9	32±9	13.0±0.1	35±4	0.036±0.014	0.021±0.006
AviNCBDpSer22-TIF2	56±6	13±3	240±80	77±8	38±6	11.0±3.	27±1	0.05±0.01	0.039±0.008

	2-state HMM			3-state HMM			
	k_{on} (μM^{-1} s^{-1})	k_{off} (s^{-1})	K_D (nM)	$k_{on,t}$ f_t (μM^{-1} s^{-1})	$k_{on,c}$ f_c (μM^{-1} s^{-1})	$k_{off,t}$ (s^{-1})	$k_{off,c}$ (s^{-1})
AviACTR-NCBD	110±7	7.10±0.04	63±4	90±6	25±0.6	5.90±0.08	32±1
AviACTR-NCBDpSer19	44±1	23±1	520±40	26.0±0.1	20.0±0.7	16±1	69±4
AviACTR-NCBDpSer22	53±2	27.00±0.02	500±20	28±7	27±5	20±1	45±6
AviTIF2-NCBD	120±10	2.70±0.07	23±2	88±8	35±6	2.20±0.07	9.2±0.7
AviTIF2-NCBDpSer19	110±8	14.0±0.4	130±5	52±2	59±1	8.7±0.1	29.0±0.3
AviTIF2-NCBDpSer22	96±4	12.0±0.1	130±6	35±1	62±5	8.0±0.1	18±1

Table S5 **C_α root-mean-square deviation (RMSD) between phosphorylated and unphosphorylated NCBD in complex with ACTR.** Difference for unphosphorylated and phosphorylated NCBD (ΔRMSD) are shown when the protein is either phosphorylated on Ser19, Ser22, or doubly phosphorylated (see Methods for details).

	$NCBD_{WT}$-$NCBD_{S19p}$ (nm)	$NCBD_{WT}$-$NCBD_{S22p}$ (nm)	$NCBD_{WT}$-$NCBD_{S19p, S22p}$ (nm)
ΔRMSD	0.3522	0.3168	0.4800

References

[1] M. Kjaergaard, K. Teilum, and F. M. Poulsen, Proc. Natl. Acad. Sci. U. S. A. **107** 12535 (2010).
[2] S. J. Demarest, M. Martinez-Yamout, J. Chung, H. Chen, W. Xu, H. J. Dyson, R. M. Evans, and P. E. Wright, Nature **415** 549 (2002).
[3] L. Waters, B. Yue, V. Veverka, P. Renshaw, J. Bramham, S. Matsuda, T. Frenkiel, G. Kelly, F. Muskett, M. Carr, and D. M. Heery, J. Biol. Chem. **281** 14787 (2006).
[4] C. W. Lee, M. A. Martinez-Yamout, H. J. Dyson, and P. E. Wright, Biochemistry **49** 9964 (2010).
[5] J. Dogan, T. Schmidt, X. Mu, A. Engstrom, and P. Jemth, J. Biol. Chem. **287** 34316 (2012).
[6] F. Zosel, D. Mercadante, D. Nettels, and B. Schuler, Nature Commun. **9** 3332 (2018).
[7] A. Waterhouse, M. Bertoni, S. Bienert, G. Studer, G. Tauriello, R. Gumienny, F. T. Heer, T. A. P. de Beer, C. Rempfer, L. Bordoli, R. Lepore, and T. Schwede, Nucleic Acids Res. **46** W296 (2018).
[8] W. Kabsch, and C. Sander, Biopolymers **22** 2577 (1983).